Politecnico di Milano
School of Industrial and Information Engineering
Master Degree in Aeronautical Engineering
Dipartimento di Scienze e Tecnologie Aerospaziali

Design, identification and control of a micro aerial vehicle

Advisor: Prof. Marco LOVERA
Co-Advisor: Eng. Mattia GIURATO
Eng. Pietro PANIZZA

Thesis by:
Daniele CHEVALLARD Matr. 841331

Academic Year 2016–2017

Alla mia famiglia, la mia fortuna più grande...

Acknowledgments

Desidero ringraziare innanzitutto il Professor Marco Lovera, l'ingegner Mattia Giurato e l'ingegner Pietro Panizza per avermi coinvolto nel progetto di ANT-1, ma soprattutto per la pazienza dimostrata e le conoscenze che mi hanno trasmesso.

Ringrazio i professionisti che hanno collaborato a questa tesi: i tecnici Luigi Negri e Matteo Tantardini, la mia carissima professoressa d'inglese Edwige Lanzerath.

Abstract

After more than one hundred years of efforts to get man airborne, aerospace engineering has increasingly dedicated itself to developing UAVs "Unmanned Aerial Vehicles". Such vehicles open up new and exciting horizons because, without the pilot presence and weight, UAVs can be miniaturised giving birth to MAV "micro aerial vehicle" sub-category.

Miniaturisation is paving the way towards an interesting possibility: the creation of aerial collective systems able to fly in cluttered environments such as cities or the insides of buildings. By working together, multiple flying robots can perform a given task quicker and more efficiently than a single system. In fact, multiple robots can share computing, sensing and communication payload so that they result faster and quicker than a unique, large UAV. Additionally, they can cover a wider area than a single aerial vehicle when flying outdoors. Thus, it is clear that aerial collective systems have a huge potential in terms of application as: monitoring of toxic clouds and meteorological conditions, security and artistic show.

The purpose of this thesis is to design a laboratory platform which can be involved in both innovative designs and teaching projects. The former refers to MAV swarming, which is our ultimate goal, while the latter points to traditional engineering issues as dynamic identification and control law design.

The thesis is structured in such a way as to cover the entire design process, from the preliminary analysis to the first ground tests. Thus, this work gives any engineering student the chance to approach RPV (remotely piloted aircraft) world analysing a MAV design from scratch. It begins with design requirements and device choice, successively the actuator and attitude dynamic are identified with an experimental campaign and validated with Matlab simulation. Finally, control design is performed using H_∞ technique which synthesize optimal control laws. Results are validated in real tests.

Sommario

Dopo più di 100 anni di studi per portare l'uomo alla conquista dei cieli, l'ingegneria aeronautica ha cominciato a dedicarsi con crescente interesse ai velivoli senza pilota, comunemente chiamati UAV: "Unmanned Aerial Vehicle". Questo tipo di velivoli apre dei nuovi ed eccitanti orizzonti per l'ingegneria aerospaziale, perchè senza l'ingombro ed il peso del pilota, possono essere miniaturizzati, dando vita alla sottocategoria dei MAV: "Micro Aerial Vehicle".

Questa caratteristica ha aperto la strada per una nuova suggestione: il volo in stormo di tanti piccoli robot, capaci perfino di volare in ambienti angusti come conglomerati urbani o l'interno di edifici. Lavorando insieme, gruppi di MAV potrebbero raggiungere un obiettivo più efficacemente rispetto a un singolo sistema. Informazioni, misure e carico pagante potrebbero essere condivise di modo che stormi di MAV risultino più sicuri e veloci rispetto ad un unico, grande UAV. Inoltre, all'aperto sarebbero in grado di coprire aree molto più vaste di quanto non potrebbe fare un unico velivolo. E' chiaro quindi che formazioni di questi piccoli velivoli avrebbero un potenziale enorme in termini di applicazione: come il monitoraggio di nubi chimiche e di condizioni meteorologiche, sicurezza e spettacoli artistici.

L'obiettivo di questa tesi è progettare una piattaforma da laboratorio che possa essere coinvolta sia in progetti innovativi, come il volo in stormo, sia in progetti didattici, come l'identificazione della dinamica o il progetto delle leggi di controllo. Inoltre è strutturata per guidare passo dopo passo la progettazione del MAV e per costruire un ambiente di sviluppo completo che copra l'intero ciclo di progettazione. In questo modo qualsiasi studente d'ingegneria potrà avvicinarsi al mondo dei velivoli a pilotaggio remoto (RPV) analizzando da zero il progetto di un MAV.

Il prototipo è stata chiamato ANT-1 ed è un quadrirotore costruito interamente con componenti rintracciabili sul mercato. Si comincerà definendo i requisiti di volo, per poi scegliere i componenti che garantiscano le performance migliori e il soddisfacimento della missione. Successivamente si identificherà la dinamica degli attuatori e di assetto attraverso simulazioni e campagne sperimentali. Infine, come ultimo step, viene presentata una metodologia per tarare i coefficienti dei regolatori, di modo che siano raggiunte le prestazioni desiderate.

Contents

List of Figures

List of Tables

Introduction

State of the art

As summerized in [11], several micro aerial platforms have been conceived. The aviation history reports that lighter than air structure represents the easiest way to get airborne, thus the first devices developed were blinds used to demonstrate flocking behaviours (Melhuish and Welsby [9]) and to create artistical shows (Figure 1).

Fixed wing UAVs are widespread due to their energy efficiency and simple mechanical design: the BlackWidow ([6]) is a successful prototype, it is represented in Figure 2. It flies using a hotwired foam rectangular wing with tapered corners, its propeller is directly driven, the electrical propulsion system is powered by lithium batteries. The MAV has a 15 cm wingspan and configuration-dependant weight of around 80g. The drawbacks are that fixed wing UAV are incapable of hovering or moving backwards and sidewards, thus making it difficult to design cooperative controllers. Moreover they can not be used in indoor environment.

This leads to microsized helicopters, but they are affected by mechanical complexity related to main and tail rotors. This is the reason why quadcopters are more attractive. Nowadays every model aircraft enthusiast could build a quadrotor, a fact which has led to a great increase in the commerce of quadcopter components. Quadcopters generally use two pairs of identical fixed pitched propeller; two clockwise (CW) and two counterclockwise (CCW). Each rotor produces both thrust and a torque. If all rotors are spinning at the same angular velocity, the angular momentum does not change, so angular acceleration does not show up. This equilibrium can be disrupted changing propeller rates, thus the produced thrust as reported in Figure 4. In case "d", a quadrotor induces yaw motion by applying more thrust to rotors rotating in one direction. In case "b" and "c", pitch or roll motion are generated by applying more thrust to one rotor and less thrust to its diametrically opposite rotor. The downside of the quadcopter with respect to fixed wing UAV is its high energy consumption due to its four high speed motors. Additionally high propeller rates reduce blade airfoil efficiency. This is why fixed wing UAVs are characterised by longer endurance.

An alternative design has been proposed: researchers are looking with increasing interest to bio-inspired airframes with flapping wings which are able to produce

both lift and forward thrust ([8]). This architecture may lead to an interesting compromise as it enables both hovering and gliding flight. The Microbat (Figure 3) is a flapping MAV which was tested using flap amplitudes from 40 to 60 degrees (comparable to flap amplitudes used by small birds). Although intended to be tailless, the complex flight control system necessary to differentially control both Microbat wings for three-axis control was abandoned for a simpler tailed design. Wings consist of electrically stimulated muscle wires. Microbat is powered by a lithium battery which can flight for 25 minutes.

Figure 1: Flocking blimps.

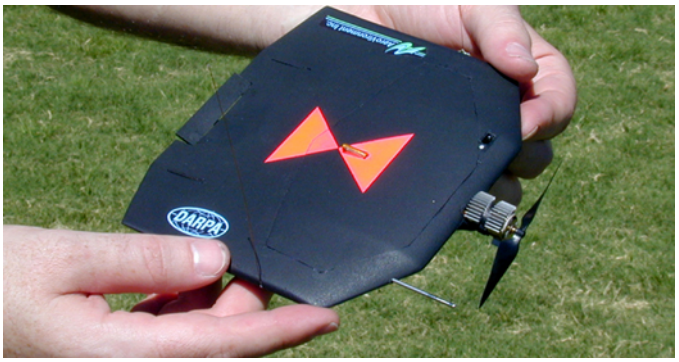

Figure 2: The DARPA Black Widow.

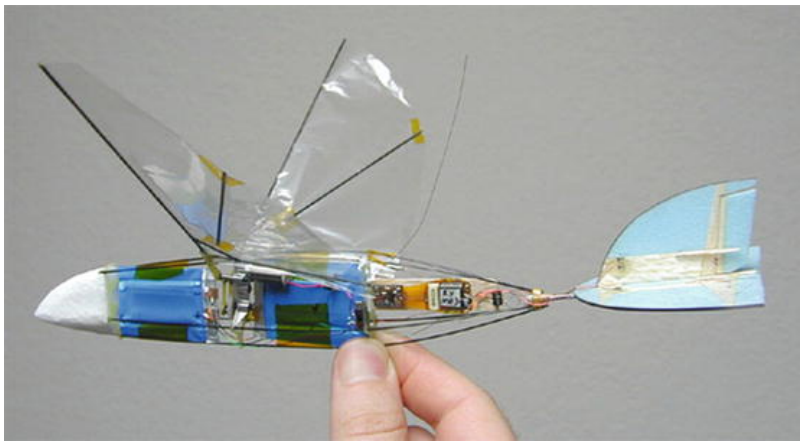

Figure 3: The flapping MicroBat.

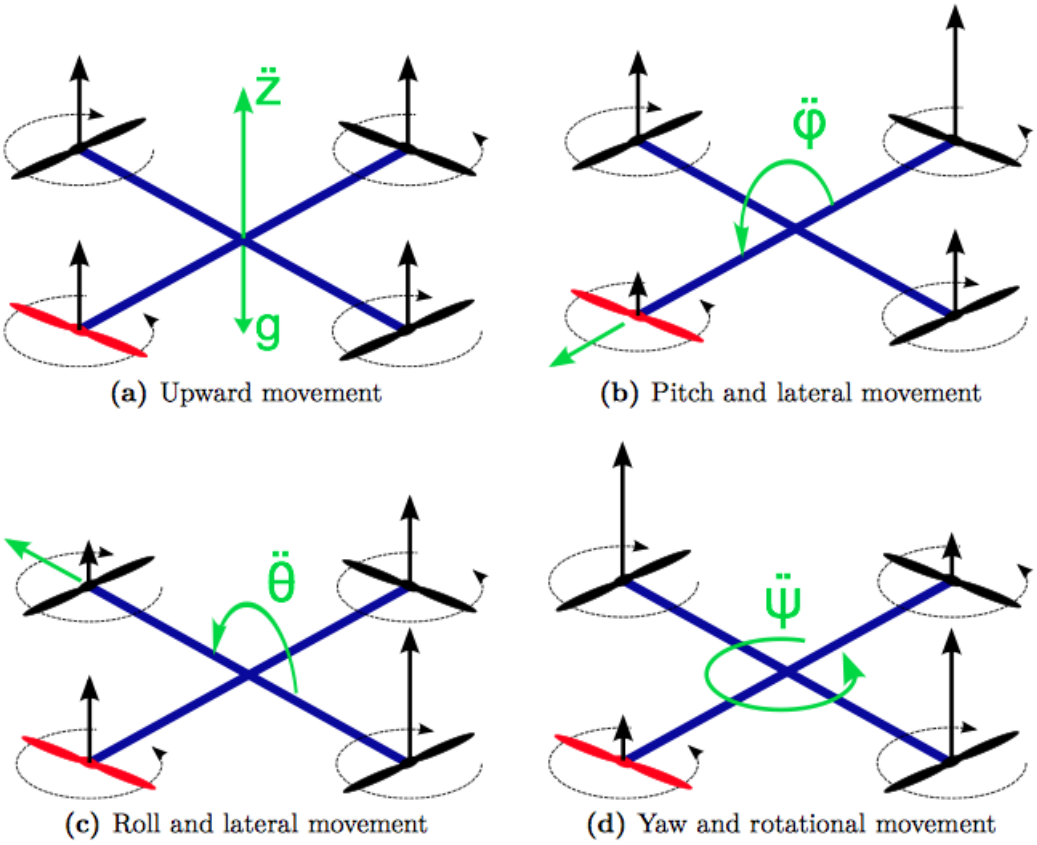

(a) Upward movement **(b)** Pitch and lateral movement

(c) Roll and lateral movement **(d)** Yaw and rotational movement

Figure 4: Quadrotor flight dynamic.

Thesis description

This thesis begins defining the design requirements and mission characteristics. According to these conditions, components could be sized by means of formulas reported by literature. However ANT-1 is built entirely with components found off the shelf, thus their characteristics are fixed and have to be analysed as a whole to predict MAV performances. Various calculators exist to perform preliminary design: eCalc has been considered the most reliable since its calculations are based on a wide list of component parameters. Then, the chosen devices are described thoroughly exposing their characteristics and structure. Finally, hardware integration is explained step by step to have a rigorous and a detailed list of procedures to build the quadrotor.

Once the MAV has been built, its dynamic can be estimated. First actuator analysis is described: reporting the theoretical base, the test instrumentations and experimental procedures. Thrust and torque non-dimensional coefficients are computed and motor dynamic is estimated with a grey box method. Results are validated with a Matlab simulation of motor response which is compared with the real data obtained by tests. Then pitch attitude dynamic is identified. An other experimental campaign is set up, designing a proper input signal to excite a desired band of frequency. Unlike actuator analysis, a black box method is adopted called PBSID: "Predictor based subspace identification".

As far as control is concerned, pitch control design is studied. First, a manually tuning is performed with an empirical method, then a H_∞ framework is used to synthesize a robust controller which gets the system closer to the desired performances. Finally, the controller parameters are validated matching the Matlab response simulation with the real one obtained in tests.

Thesis structure

This thesis follows a systematic approach defined in [4], that in detail consists in these steps:

- Defining mission characteristics and design requirements.
- Choice of components according to predicted performances by eCalc.
- MAV hardware integration following a list of procedures.
- Actuator non dimensional coefficients are computed and their dynamic response is identified with an experimental campaign.
- Pitch attitude dynamic identification is conceived and experimentally estimated to obtain a reliable model of ANT-1 along pitch and roll axes.

- H_∞ technique is adopted to tune regulator parameters so that control design requirements are achieved.
- The obtained control laws are validated in real test and compared with simulation provided by Matlab.

Chapter 1

Hardware design and integration

ANT-1 has been built with components found off the shelf. In the first and second sections the way such components have been chosen is exposed, moreover they are described in detail. In the third section, ANT-1 assembly is described step by step.

1.1 Preliminary analysis

ANT-1 contemplates following requirements:

- Maximum take-off weight (MTOW): less than 300 grams (to respect ENAC standards for RPV vehicles [2]).
- Flight time: at least 10 minutes.
- Reduced geometric dimension: an inter axis smaller than 200 mm.

As mentioned before, ANT-1 is built with components found off the shelf whose parameters are fixed, so preliminary analysis can not be performed with optimisation methods reported in literature. It is necessary to recur to eCalc, an on-line calculator which can predict a series of interesting performances by typing component parameters provided by manufacturer data sheets. Several configurations have been simulated: the best compromise among weight, flight time and thrust to weight ratio establishes which hardware elements to choose, listed in Table 1.1. In Figure 1.1, optimal results are reported.

Indicators show proper performances except for hovering flight time and specific thrust. The lower limit of the first parameter is 12 minutes, so 11,9 minutes is not considered a critical issue. Regarding specific thrust, this parameter is an indication of overall hover efficiency and is measured as the ratio between thrust and electric input power at the motor. More efficient solutions could be conceived but they would need a propeller of at least 5 inches, which would mean a longer frame and more weight thus going beyond design requirements. Hence, such defects are not considered severe and are neglected.

Component Type	Component Name	Weight [g]
FCU	Pixfalcon	9
Companion Computer	Raspberry Pi Zero W	15
Battery	Turnigy Nano-tech 950mah Lipo Pac	69
Motors	QAV1306-3100KV brushless Motor	12
Esc	ZTW Spider Series 18A	5.6
Propeller	Gemfan Bullnose Polycarbonate 3035 3 blade	4

Table 1.1: Hardware components.

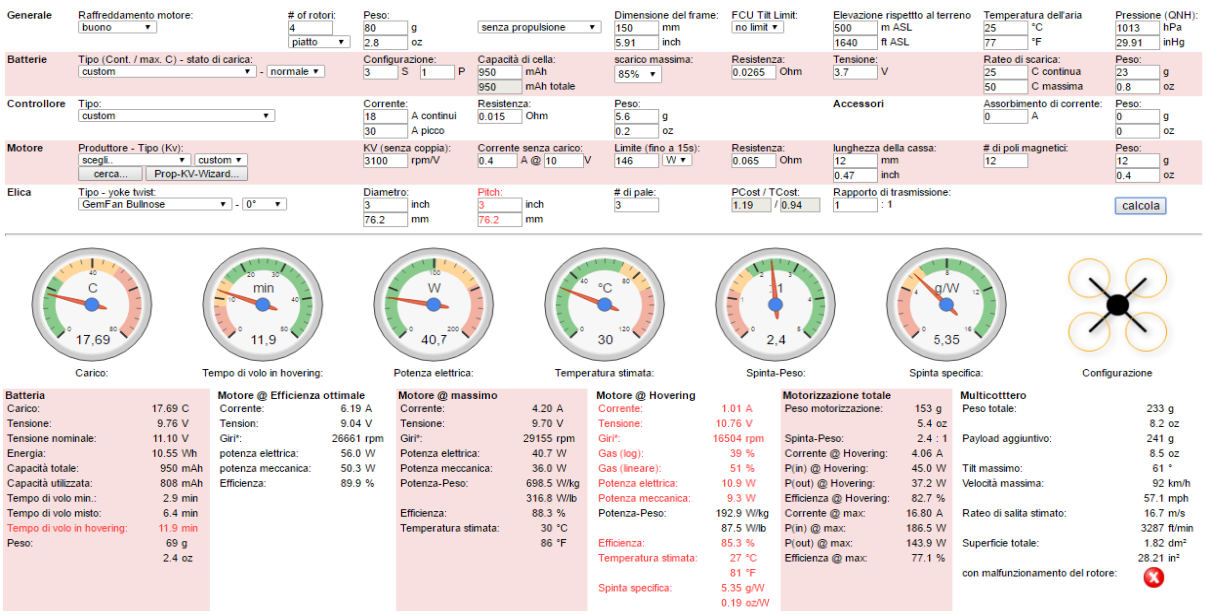

Figure 1.1: eCalc results.

1.2 Description of components

1.2.1 Pixfalcon and Raspberry Pi Zero W

The Pixfalcon board can be considered as ANT-1 FCU (Flight Control Unit). This is a low cost and open autopilot shield, suitable for RC (remotely controlled) vehicles such as quadrotors and fixed wing aircrafts. It is equipped with a 3 axes accelerometer, a 3 axes gyroscope, a magnetometer and a pressure sensor. Pixfalcon has 8 channels of PWM outputs in which ESCs can be connected. Additionally GPS can be mounted extending autopilot capabilities. Through data received by sensors, Pixfalcon is able to estimate state variables and to exert control actions.

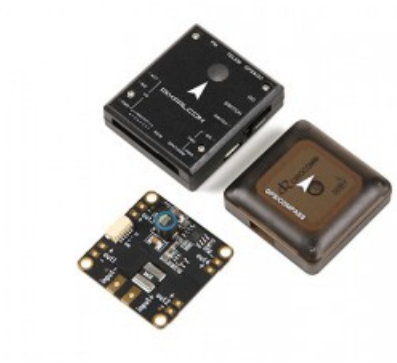

Figure 1.2: PxfMini.

The Pixfalcon is connected to a Raspberry Pi Zero W (Figure 1.3) which is a small and light single board computer. It is equipped with a Broadcom system on a chip (SoC), that includes an 1 GHz ARM compatible central processing unit (CPU) and an on-chip graphics processing unit (GPU). It can rely on 512 MB SDRAM and is characterised by a Micro-USB 2.0 port and mini-HDMI video output. Raspberry is responsible for the communication, in fact it connects to the laboratory LAN network through WI-FI, allowing ANT-1 to be controlled from the ground station. Moreover, due to its computational power, it is going to have a primary role in collaborative flight when ANT-1 will be involved in MAV swarming.

Figure 1.3: Raspberry Pi Zero W.

1.2.2 Motor, ESCs and propellers

In aeromodeling, Brushless DC motors are becoming more and more popular due to higher power to weight ratio, smaller size, reduced noise and maintenance absence. The term brushless DC name can be deceitful, in fact these devices are synchronous electric motors, thus fed by an AC signal. ANT-1 is equipped with four RcInPower QAV1306-3100KV motors (Figure 1.4a). This 12 gram motor is typically used in FPV (First Person View) racing drones because it ensures high performance with small weight.

ESCs (Electronic Speed Control) stand halfway between the battery and the motor, receiving battery DC voltage and producing a three phase switching electric signal (aforementioned AC signal). These devices generally accept a nominal 50 Hz PWM servo input signal from the FCU (so every 20 ms) whose pulse width varies from 1 ms to 2 ms. When supplied with a 1 ms width pulse, the ESC responds by turning off the motor attached to its output. A 1.5 ms pulse-width input signal drives the motor at approximately half-speed and finally a 2.0 ms input signal, makes the motor run at full speed.

The ZTW Spider Series 18A (Figure 1.4b) has been chosen due to its weight of only 5.6 grams. This device is able to modulate a 30 A current.

(a) RcInPower QAV1306-3100KV.

(b) ZTW Spider Series 18A.

(c) Gemfan BullNose 3035.

Figure 1.4: ANT-1 drive components.

Regarding propellers, longer blades are more efficient in hovering and produce higher thrust, but lead to slower control response and higher power consumption. In this project a rotor diameter of 3 inches (76 mm) has been chosen in so far as its small frame size does not interfere with central structure (Figure 1.4c). Smaller propellers present higher pitch and more than two blades to compensate aerodynamic force reduction. In this project the pitch is equal to 3.5 inches (88 mm).

1.2.3 Battery

Li-Po batteries have just taken over in radio controlled aerial vehicles because of their lower weight, variety of sizes, increased capacity and power delivery.

Capacity is the amount of electric charge a battery can deliver at the rated voltage. It is typically expressed as the amount of current it can deliver in one hour. The more electrode material is contained in the cell the greater is its capacity and (unfortunately) its weight. In order to limit weight, the Turnigy Nano-tech 950 mAh battery (Figure 1.5) has been chosen. It is characterised by 25-50 continuous and burst discharge rate, another important parameter defined as the discharge current divided by the theoretical current draw in one hour. In Figure 1.1 one can that see maximum current required at maximum power by four motors is equal to 16.80 A, since continuous discharge rate is equal to 25, the battery can supply 23.75 A which is sufficient for the requested current.

Figure 1.5: Li-Po battery.

1.2.4 Frame

It is possible to find several types of frames off the shelf. They are characterised by optimal weight values and attractive mock up, but they lack adaptability. In fact commercial casings are typically designed for specific batteries, motors and FCUs. Having started the project choosing those component, a self design frame is needed.

Design requirements are:

- Reduced weight: less than 40 grams.
- Adaptability to Pixfalcon, Raspberry and QAV1306-3100KV motors.
- Reduced geometric dimensions: an inter axis (distance between opposites motors) smaller than 200 mm.
- Crash resistance.

To respect geometric constraints, a cross plate with 160 mm inter axis has been conceived (Figure 1.6). The Pixfalcon and Raspberry boards are supported by an upper part which presents associated holes (Figure 1.7). The chosen material is plywood for test frames, while the definitive ones are made of carbon fiber. Such a material ensures strength at low weight (30 grams). The test frame is represented in Figure 1.8.

Figure 1.6: Cross plate.

1.2.5 Power module

Power is distributed from the battery to the UAV devices by means of a power module. This device is also linked with the Pixfalcon so that the battery current can be measured to send low battery messages to the user (Figure 1.9).

Figure 1.7: FCU and Raspberry support.

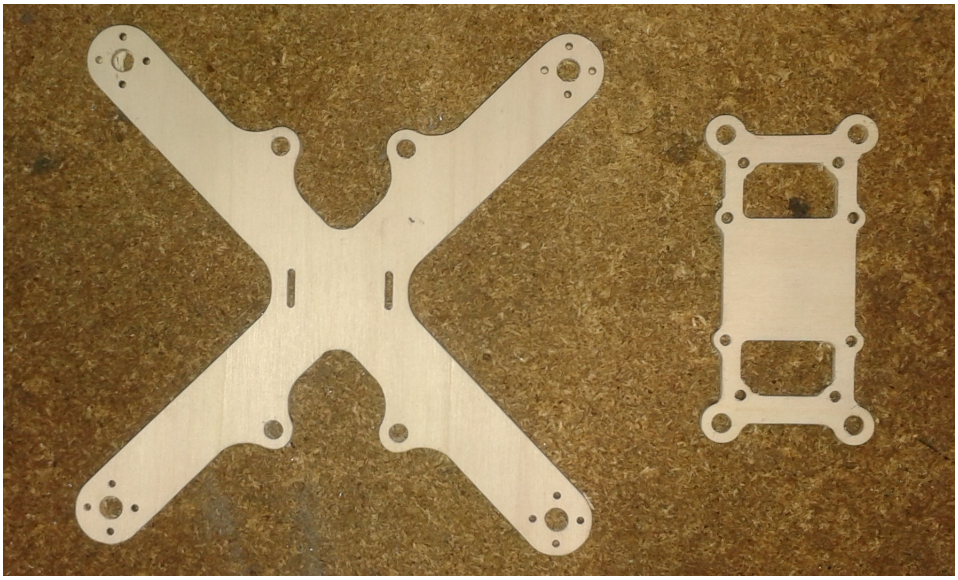

Figure 1.8: Prototype frame.

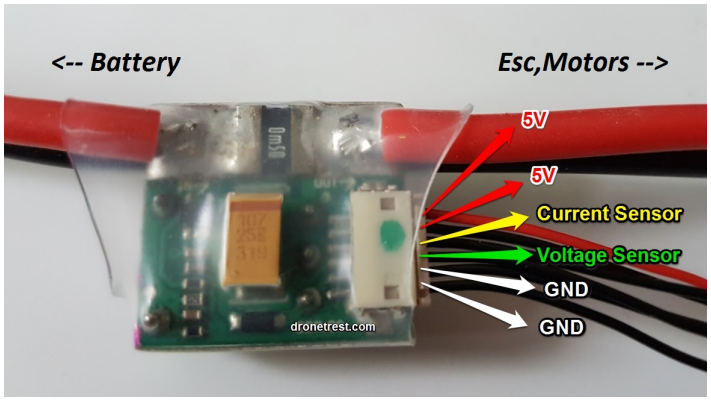

Figure 1.9: Power module.

1.2.6 Remote controller

ANT-1 is controlled by means of attitude set point messages sent by two sources: ground control station and manual controller (Figure 1.10). The goal is to use ground control station to fly, while the manual controller connection is set for safety reasons. In fact, if something goes wrong, ANT-1 can be promptly disarmed through a manual controller switch.

Figure 1.10: Remote controller.

1.3 Hardware Integration

1.3.1 Motor and ESC

The first step consists in welding each motor to ESC as reported in Figure 1.11. The three black wires provide three phase current to the motor. Regarding ESC two outer wires are jointed to the power module as described in section 1.3.2, providing DC battery current. The central coupled wires are connected to Pixfalcon, which sends inputs to the motor in accordance to its control laws.

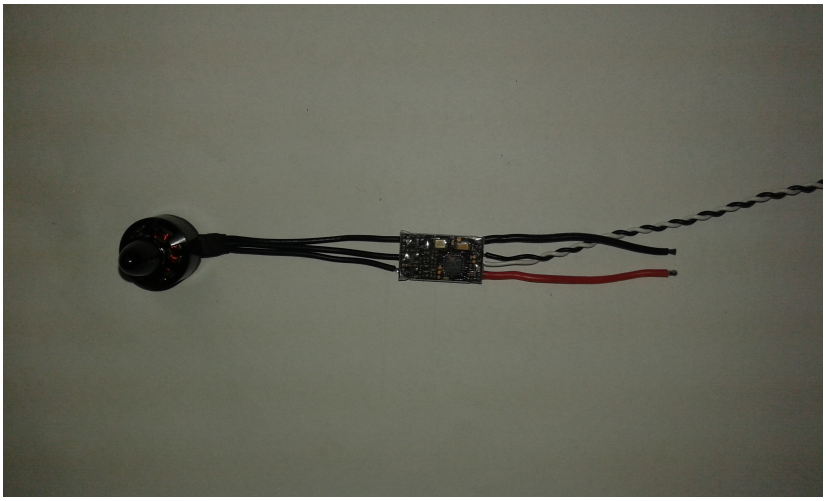

Figure 1.11: Welded motor and ESC.

1.3.2 Power module

The electrical power has to flow from the battery to the electrical devices: the power module is responsible for this energy distribution. In Figure 1.12 the electrical scheme is sketched.

The battery and ESC red wires have to be welded in the upper part of the power model, while the black wires are jointed to the lower part (Figure 1.13). Battery current is computed as ratio of voltage sensor measurement and known resistance:

$$\hat{I} = \frac{V_{sensor}}{R_{known}}$$

1.3.3 Frame

Motors are mounted on the frame through four screws. It is highly recommended to fix the ESCs with some tape. The battery and the power module are attached with felt passing through dedicated slots at frame core.

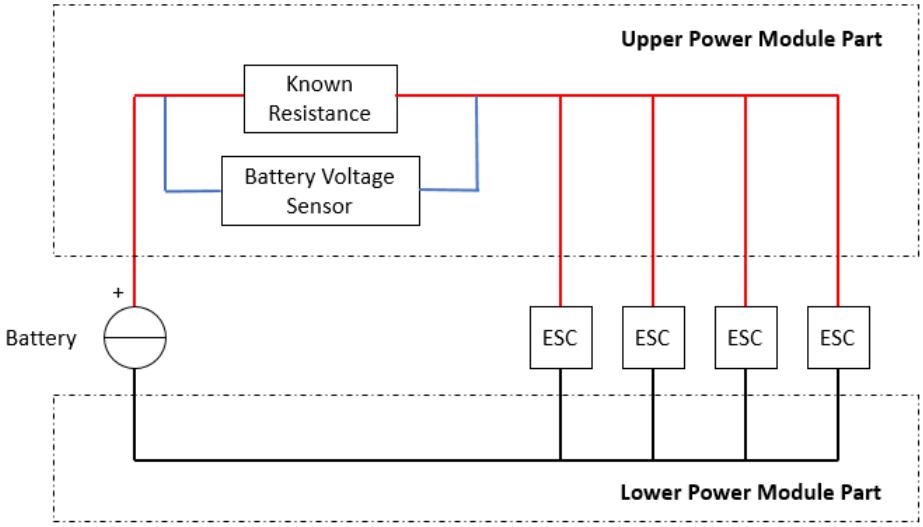

Figure 1.12: Power module electrical scheme.

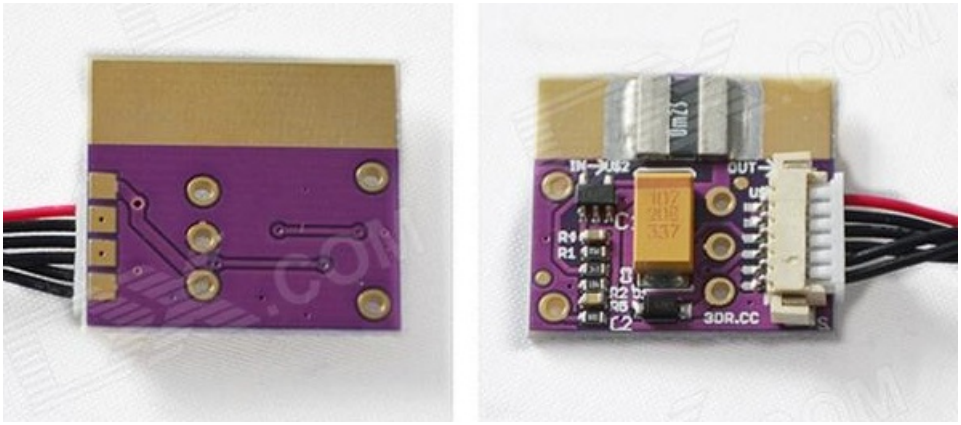

Figure 1.13: Down and top view of the power module.

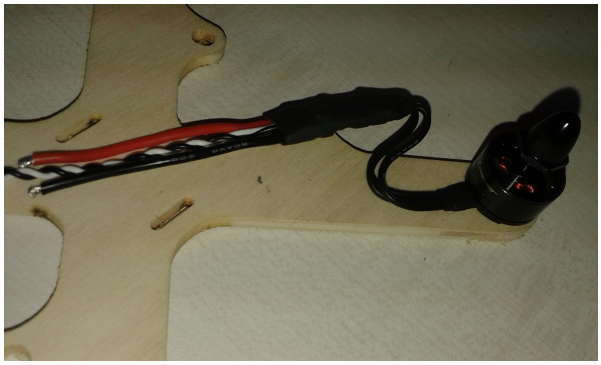

Figure 1.14: Motor and frame.

The frame presents 4 holes conceived for damper balls (Figure 1.15), which sustain the upper part and reduce any vibration transmitted to FCU. In fact brushless DC motors induce persistent vibrations that can disturb sensors in FCU. Thus, damper balls have to be inserted in such holes. This procedure has to be repeated with the upper plateau.

Figure 1.15: Damper balls.

1.3.4 Upper plateau

The upper plateau is characterised by four internal and external holes. Internal ones are used to joint the Pixfalcon, while the external ones to fix Raspberry. These devices are constrained through spacer screws, which present a slot on one side and a thread on the other side, as reported in Figure 1.16. They are conceived to space parts in addition to their traditional use.

1.3.5 Conclusions

Final configuration weights only 230 grams and is characterised by a 160 mm inter axis. Reduced dimensions make ANT-1 suitable for MAV swarming while Raspberry enables the communication and collaboration with other flying robots.

Figure 1.16: Spacer screws.

Chapter 2

Actuator analysis

Non-dimensional coefficients are usually adopted in aeronautical engineering to compare rotors characterised by different features. In this chapter C_T, C_P and C_Q are estimated through a test-bed designed for the ANT-1 specific case. Additionally propeller rates associated to throttle percentages and dynamic response between real rate values and reference ones are evaluated.

At first the theoretical base is illustrated, then test instrumentation and procedures are described and finally data elaboration and results are shown.

2.1 Propeller model

2.1.1 Momentum theory analysis in hovering flight

During the tests, the motor is bound to the test bed described in Section 2.2.3, so hovering flight condition can be assumed. Typically this flight regime is analysed first and should be the easiest one to predict by means of mathematical models. Unfortunately, it has been found that even through advanced numerical computations, it is arduous to fully describe flow in this condition. However, as a first step, basic rotor performances can be achieved by Rankine-Froude momentum theory which introduces some simplifications that reduce aforementioned complications. This theory assumes to deal with:

- Incompressible and ideal fluid: that is, no compressibility effects show up and no viscous shears between fluid elements are present.
- Quasi-steady fluid: which means flow characteristics in a specific point do not change with time.
- One dimensional flow: namely its properties do not change along planes parallel to rotor disk.
- Infinite number of blades of zero thickness: which compose an actuator disk over which a pressure difference exists.

As stated in [5], the actuator disk supports the thrust force that is generated by the rotation of the rotor blade about the shaft. Power is required to generate this thrust, which is supplied in form of a torque to the rotor shaft. Through conservation laws of aerodynamic, Rankine-Froude momentum theory asserts this thrust and power expressions:

$$T = 2\rho A {v_i}^2, \tag{2.1}$$

$$P = T v_i = 2\rho A {v_i}^3. \tag{2.2}$$

where ρ, A, v_i refer respectively to air density, disk area, induced velocity by rotor.

2.1.2 Buckingham π theorem

Adimensional coefficients can be provided by Buckingham theorem which asserts every physical equation such as:

$$f(q_1, q_2, ..., q_n) = 0, \tag{2.3}$$

where $q_1, q_2, ..., q_n$ are the n physical variables, expressed in terms of the k independent physical variables units, can be restated as a function of the $n-k$ adimensional groups π_j in this way:

$$g(\pi_1, \pi_2, ..., \pi_{n-k}) = 0. \tag{2.4}$$

π_j can be composed by original variables as follows:

$$\pi_j = q_1^{e_{j1}} q_2^{e_{j2}} ... q_k^{e_{jk}} q_{k+j} \qquad j = 1, ..., n-k. \tag{2.5}$$

where e^{jk} are chosen so that adimensionalisation is imposed.

So, remembering it is a rotor-craft aircraft convention to adimensionalise all velocities by blade tip speed in hovering flight ($v_{tip} = \Omega R$), (2.1) can be rewritten in this functional form:

$$f(T, \rho, A, v_{tip}, v_i) = 0, \tag{2.6}$$

where $n = 5$. ρ, A, v_{tip} are chosen as independent dimensions since they refer respectively to mass, length and time. Thus, because $k = 3, n-k = 2$, (2.6) can be re-written in form of 2 adimensional groups:

$$g(\pi_1, \pi_2) = 0, \tag{2.7}$$

where π_1 is called "thrust coefficient" and defined as:

$$\pi_1 = \rho^{-1} A^{-1} {v_{tip}}^{-2} T = \frac{T}{\rho A \Omega^2 R^2} = C_T, \tag{2.8}$$

while π_2 is called "inflow ratio" and defined as:

$$\pi_2 = \rho^0 A^0 {v_{tip}}^{-1} v_i = \frac{v_i}{v_{tip}} = \lambda_i. \tag{2.9}$$

By (2.8) is possible to obtain torque and power coefficients, namely C_Q, C_P

$$C_P = \frac{P}{\rho A {v_{tip}}^3} = \frac{P}{\rho A \Omega^3 R^3}, \tag{2.10}$$

$$C_Q = \frac{Q}{\rho A {v_{tip}}^2 R} = \frac{Q}{\rho A \Omega^2 R^3}. \tag{2.11}$$

It should be noted that since power can be evaluated as $P = \Omega Q$, it results $C_P = C_Q$.

2.2 Test instrumentation

To estimate C_T, C_Q, the thrust and torque curves have to be obtained as a function of the propeller rate. To full-fill this aim, the following instruments are needed.

2.2.1 Load cell

In this test a strain gauge load cell (Figure 2.1a) is adopted to evaluate thrust. This kind of sensor creates an electrical signal whose magnitude is directly proportional to strain induced by load. To read sensor output an INstrumentation Amplifier (INA) is required and has to be linked to the load cell as represented in Figure 2.1b. Gathered data are logged with a low-cost Arduino Uno electronic board.

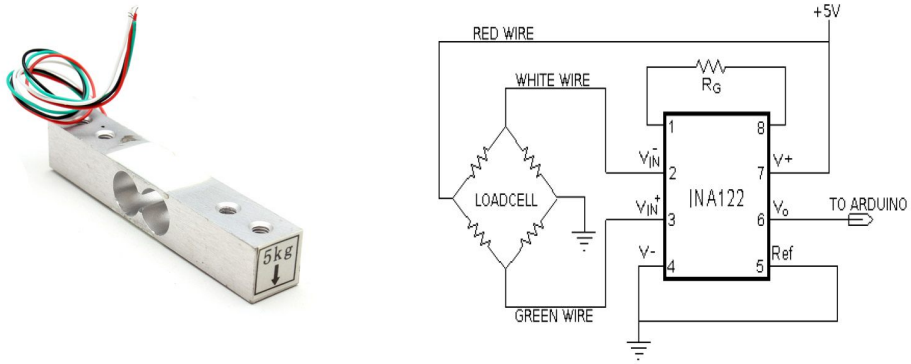

(a) Strain gauge load cell. (b) INA.

Figure 2.1: Load cell.

2.2.2 Oscilloscope

The static relationships between the throttle percentages and the propeller rates are measured by the combination of a laser source and a photodiode sensor (Figure 2.2). The laser beam collides the photodiode which operates as a switch making the current flow. If the photodiode is not hit by the laser beam the output is equal to 0 V (LOW), otherwise a 5 V (HIGH) signal is measured. In this way, by a propeller located between the light source and the photodiode, a periodic signal is generated. Through an oscilloscope its shape can be appreciated and so can its frequency (Figure 2.3) which corresponds to the rotational speed. It should be noted that the oscilloscope does not measure the propeller rate but the blade rate, because it has not in knowledge of a 3 blade propeller being tested. To obtain the propeller period, the blade period has to be multiplied by 3.

(a) Laser source. (b) Photodiode.

Figure 2.2: Rate sensors.

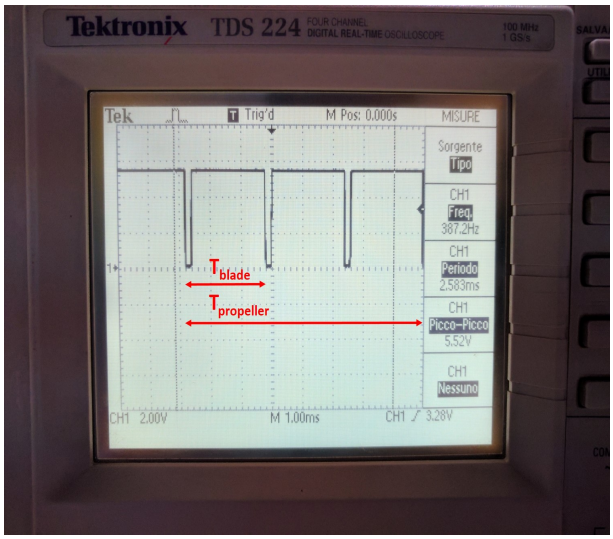

Figure 2.3: Oscilloscope.

2.2.3 Test-bed

A test bed (Figure 2.4) is designed to evaluate thrust and torque avoiding ground effect and interferences with structural parts. To achieve this aim the motor and the rotor are far from the base and the nearest column respectively by a height of 220 mm and a length of 200 mm. Thrust is evaluated by screwing the motor to a plateau which is fixed to the load cell. The plateau is stiff enough to avoid being deformed by strains and allows to allocate loads to sensor. To measure the motor counter torque, a "L" part is free to rotate about a prominent cylinder. A screw is used to push on a digital scale to have a reading of V which is related to counter torque C as described in (2.13).

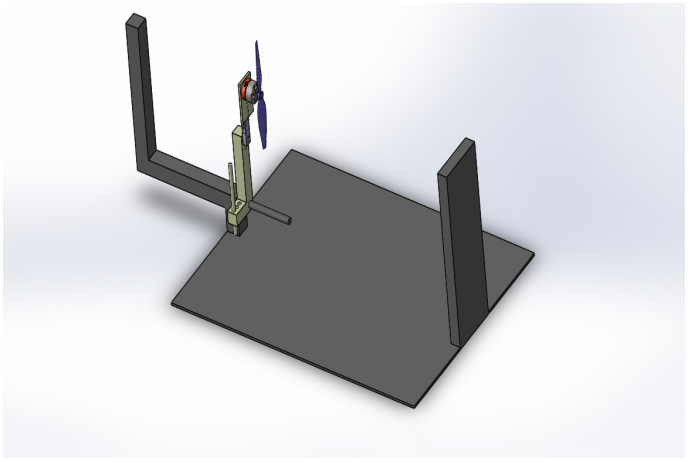

(a) Conceptual test bed design.

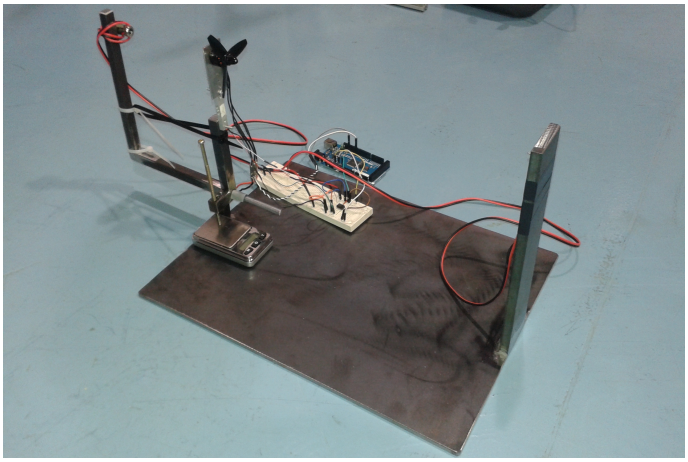

(b) Real test bed.

Figure 2.4: Test-bed.

2.3 Conservation laws

By horizontal equilibrium, thrust can be evaluated as represented in Figure 2.5.

$$\sum F = 0 \tag{2.12}$$

$$T = H$$

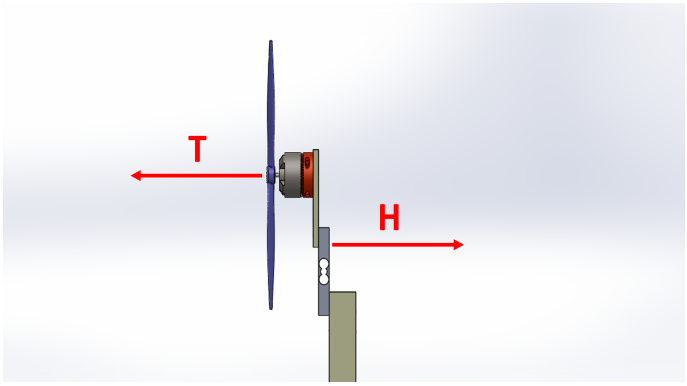

Figure 2.5: Thrust physical scheme.

Regarding torque, rotational equilibrium with respect to hinge is invoked. It should be noted that center of gravity does not lie on the hinge vertical, but shifted slightly to the left, exerting a M_G moments. Thus, by evaluating the difference between scale measurements before and after the motor starts, C can be obtained (Figure 2.6).

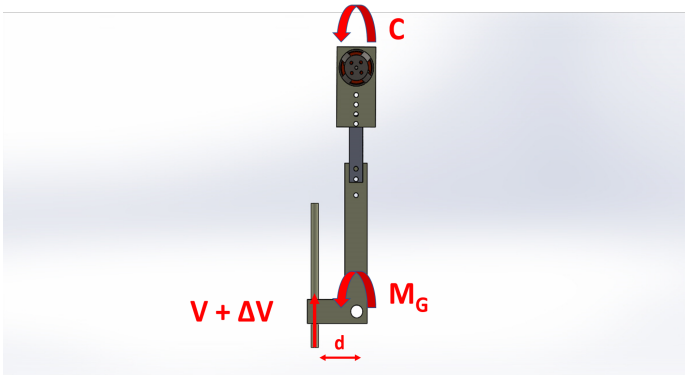

Figure 2.6: Torque physical scheme.

$$\sum M = 0$$

$$Engine\ OFF : V \cdot d = M_g$$

$$Engine\ ON : (V + \Delta V) \cdot d = M_g + C$$

$$C = \Delta V \cdot d \tag{2.13}$$

2.4 Static response estimation

A typical parameter estimation problem is characterised by a large number of tests performed to estimate few parameters. In mathematical terms, this situation leads to an over determined system, which can be written as:

$$\begin{pmatrix} y_1 \\ y_2 \\ \vdots \\ y_m \end{pmatrix} = \begin{bmatrix} X_{11} & \dots & X_{1n} \\ X_{21} & \dots & X_{2n} \\ \vdots & \vdots & \vdots \\ X_{m1} & \dots & X_{mn} \end{bmatrix} \begin{pmatrix} \beta_1 \\ \vdots \\ \beta_n \end{pmatrix}, \tag{2.14}$$

Where y refers to measurements while β refers to parameters, thus $m > n$. The least squares method provides the optimal solution for such a problem based upon minimisation of a cost function composed by the sum of squares of errors between the real values and the fitted ones.

$$J(\beta) = \sum_{i=1}^{m} [y_i - \sum_{j=1}^{n} X_{ij}\beta_j]^2, \tag{2.15}$$

Provided that n columns of the matrix X are linearly independent, by derivation of J in term of β, $\hat{\beta}$ parameters can be estimated.

$$\hat{\beta} = (X^T X)^{-1} X^T y. \tag{2.16}$$

Since linear relation between $Th_{\%}$ and Ω is expected, the estimation problem is formulated and solved in this fashion:

$$\Omega = \hat{m} Th_{\%} + \hat{q} \qquad \rightarrow \qquad y = \begin{pmatrix} \Omega_{10} \\ \Omega_{20} \\ \vdots \\ \Omega_{100} \end{pmatrix}, X = \begin{bmatrix} Th_{10} & 1 \\ Th_{20} & 1 \\ \vdots & \vdots \\ Th_{100} & 1 \end{bmatrix}, \hat{\beta} = \begin{pmatrix} \hat{m} \\ \hat{q} \end{pmatrix}, \tag{2.17}$$

$$\begin{pmatrix} \hat{m} \\ \hat{q} \end{pmatrix} = (X^T X)^{-1} X^T y. \tag{2.18}$$

As mentioned in Section 2.1.1, thrust and torque are related with propeller rate as (2.19) and K_T, K_Q are defined as:

$$T = K_T \Omega^2, \qquad Q = K_Q \Omega^2, \tag{2.19}$$

$$K_T = C_T \rho A R^2, \qquad K_Q = C_Q \rho A R^3.$$

Thus it is apparent K_T, K_Q are parameters that have to be estimated and that $\hat{C_T}$ and $\hat{C_Q}$ are computed as reported in 2.21. Since problem structure does not change, only the thrust case is exposed:

$$y = \begin{pmatrix} T_{10} \\ T_{20} \\ \vdots \\ T_{100} \end{pmatrix}, X = \begin{pmatrix} \Omega_{10}^2 \\ \Omega_{20}^2 \\ \vdots \\ \Omega_{100}^2 \end{pmatrix}, \hat{\beta} = K_T, \tag{2.20}$$

$$\begin{aligned} \hat{C_T} &= \frac{K_T}{\rho A R^2}, \\ \hat{C_Q} &= \frac{K_Q}{\rho A R^3}. \end{aligned} \tag{2.21}$$

2.5 Dynamic response estimation

In this section the dynamic response between reference propeller rate values and actual ones are estimated. A grey-box method is adopted since typically actuator dynamic is modelled with a first order transfer function. Sixty tests have been performed as listed in Table 2.1.

Throttle Steplike Input	Number of Test
from 20% to 40%	10
from 40% to 20%	10
from 40% to 60%	10
from 60% to 40%	10
from 60% to 80%	10
from 80% to 60%	10

Table 2.1: Dynamic response estimation test.

In these tests rates are not obtained from the oscilloscope since data can not be logged, but from the thrust measurements according to (2.22).

$$\Omega = \sqrt{\frac{T}{K_T}}. \tag{2.22}$$

An early design plans an Arduino analogic measurement of the periodic signal generated by propellers, but Arduino results to be too slow for accurate high RPM readings. This is probably related to the fast engine rates which does not allow Arduino to complete its operations.

2.6 Experimental results and conclusion

As far as static response is concerned, the identification campaign leads to the following aerodynamic coefficients:

$$\begin{cases} \hat{C_T} = 2.176 \times 10^{-2} \\ \hat{C_Q} = 2.067 \times 10^{-3} \\ \hat{C_P} = 2.067 \times 10^{-3} \end{cases} \tag{2.23}$$

While regarding the static relationship between $Th_{\%}$ and Ω:

$$\Omega = \hat{m} Th_{\%} + \hat{q} \rightarrow \begin{cases} \hat{m} = 26.584 & [\frac{rad}{s}] \\ \hat{q} = 683.124 & [\frac{rad}{s}] \end{cases} \tag{2.24}$$

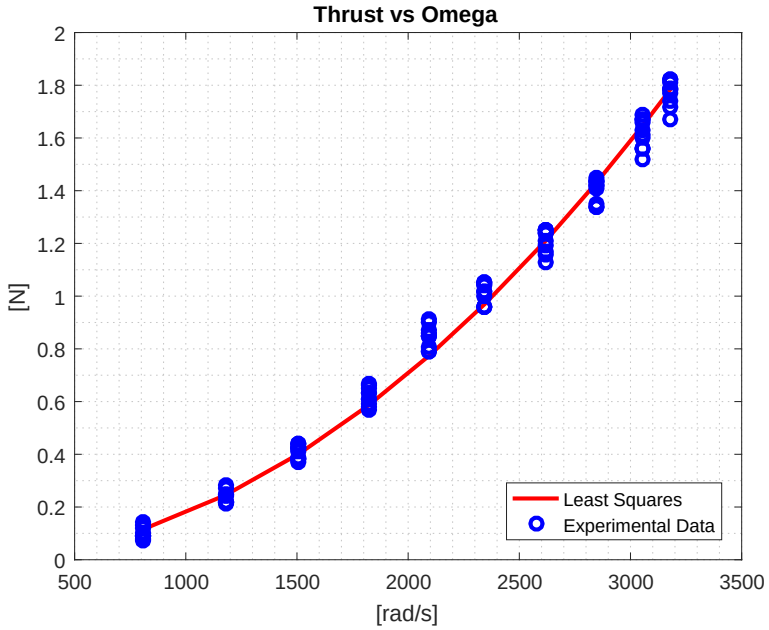

Figure 2.7: Static relationship between thrust and Ω.

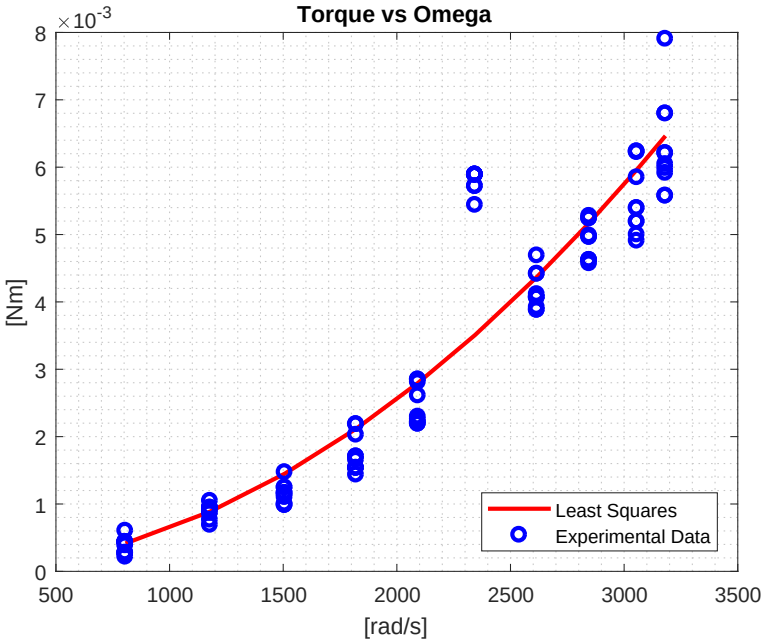

Figure 2.8: Static relationship between torque and Ω.

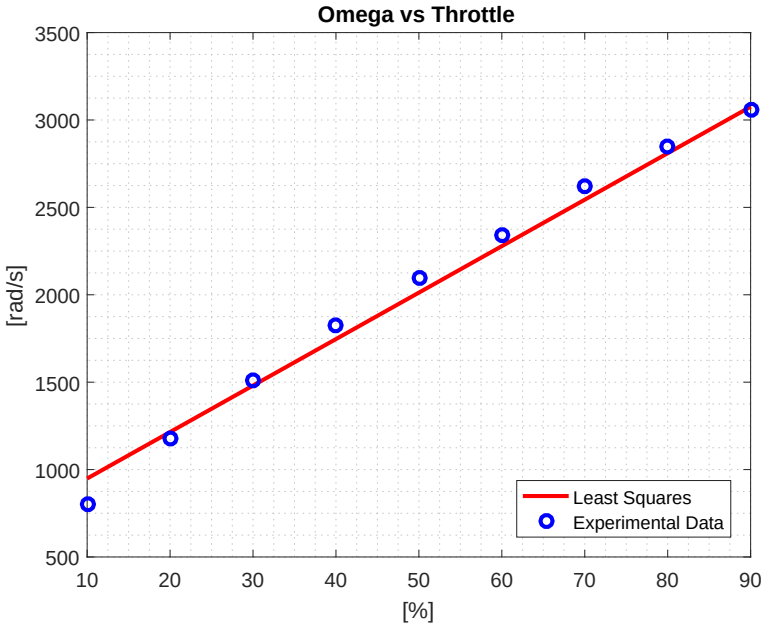

Figure 2.9: Static relationship between $\mathrm{Th}_{\%}$ and Ω.

The thrust and torque quadratic trends described by Momentum Theory Analysis are verified and so is linear relationship of $Th_{\%}$. An anomaly at Throttle 60% in Figure 2.8 can be noticed. Since the propeller rate is almost 2500 rad/s over here, it is somewhat possible that a structural natural frequency has been touched on. In fact during the test a different sound can clearly be heard at this throttle percentage. As far as the dynamic response is concerned, a first order transfer function is verified. Its parameters (2.25) are estimated and simulated with Matlab as reported in Figure 2.10.

$$\begin{cases} \mu = 0.957 \\ \tau = 0.043 \end{cases} \tag{2.25}$$

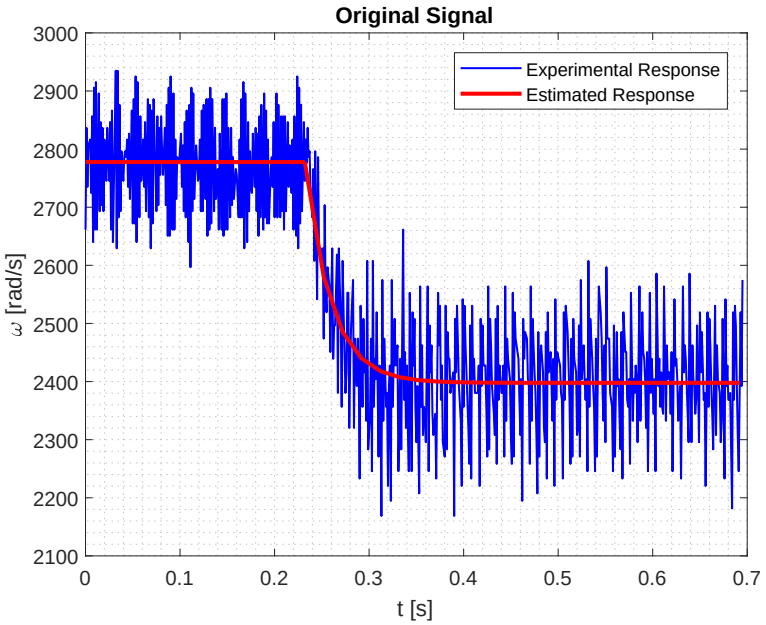

Figure 2.10: Original dynamic response.

Chapter 3

Pitch attitude identification

To design control law for attitude and position, the ANT-1 dynamic has to be identified. Since the input-output relation is unknown and can not be supposed, a black box model identification has to be adopted.

First a block scheme of the system is introduced, then the test facilities and the procedures are described in detail, finally the results are analysed. This chapter is focused only on the pitch dynamics identification, its results can be extended with some approximations to the roll axis due to ANT-1 symmetry in terms of weights distribution.

3.1 Physical model

Analysed real system can be summarized through a scheme block as represented in Figure 3.1. "R blocks" refer to controllers which are exposed in the next chapter, while "G blocks" define the processes. G_θ is a simple integrator block, G_q is the system that has to be identified. It receives a moment M as input and returns a pitch rate q as output.

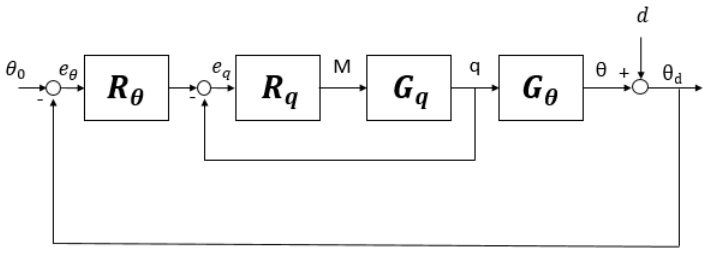

Figure 3.1: Physical model block scheme.

3.2 Test facilities and procedures

3.2.1 Test bed

Pitch attitude identification tests are performed with the test bed shown in Figure 3.2. It constrains the translational motions and the rotational DoFs except for pitch rate, moreover it keeps the UAV far from the ground to avoid ground effect. Due to this test-bed configuration, a hovering flight regime has to be assumed. Hence it is necessary to limit the pitch angle excursion so that the test results can be extended to a real hovering condition.

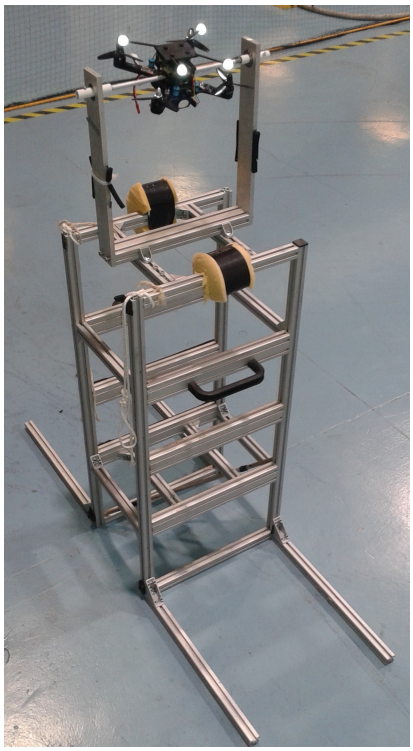

Figure 3.2: Pitch attitude identification test bed.

3.2.2 Test procedure

First of all it is necessary to guess the bandwidth to be excited in order to find actual model of the system. Typically, conservation laws are invoked and natural frequencies are analytically computed to excite system in a range that contain such a frequency. Unfortunately UAV physical models reported by literature are not suitable for the ANT-1 case due its limited dimensions, hence a bandwidth has to be supposed and validated with identification results. The exciting band upper limit is fixed at 50 rad/s. As far as amplitude is concerned, the input moment is not defined in Nm but with a normalised value between -1 and 1. For

the execution of the tests, three different amplitudes have been chosen as listed in Table 3.1.

It has been decided to excite the system with a random binary sequence (RBS): a signal that assumes two values randomly with a harmonic content similar to white noise, as reported respectively in Figure 3.3 and in Figure 3.4.

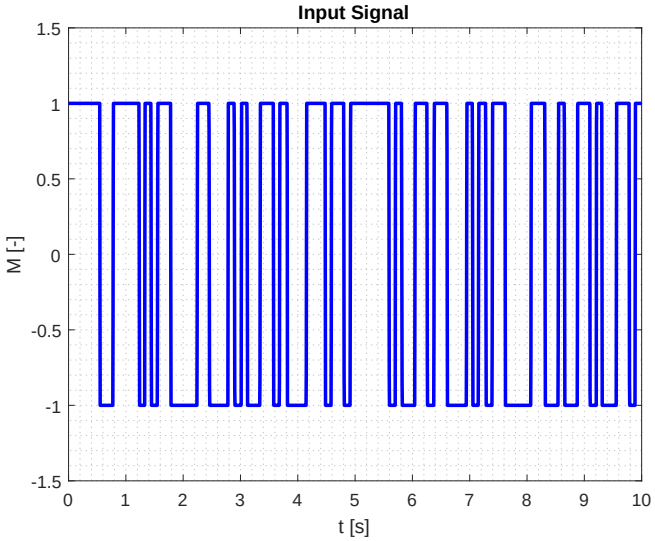

Figure 3.3: Input signal shape.

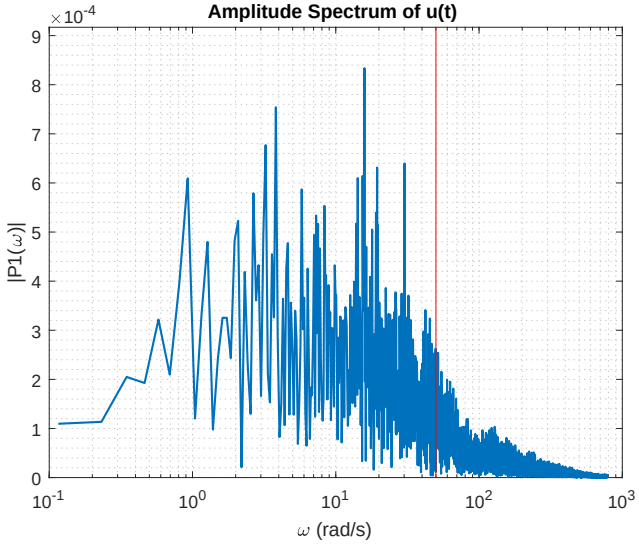

Figure 3.4: Input harmonic content.

Three tests of 20 seconds are performed for each amplitude, then the input and output data are collected together. In this way the data set is longer and can be considered more valuable.

Amplitude [-]
0.01
0.007
0.004

Table 3.1: Input signal amplitude.

Once the system is identified, its quality has to be quantified. So other three tests for each amplitude are performed. This phase of the pitch identification is called "validation process" and consists in calculating the VAF parameter (variance accounted for) which is defined as (3.1).

$$VAF = max\left(1 - \frac{variance\ (y_{real} - y_{est})}{variance\ (y_{real})}, 0\right) \cdot 100. \tag{3.1}$$

y_{real} and y_{est} are generated feeding the real system S_{real} and the identified system S_{est} with the same input u, as reported in Figure 3.5. The VAF of two signals that are the same is 100%, while if they differ, the VAF will be lower.

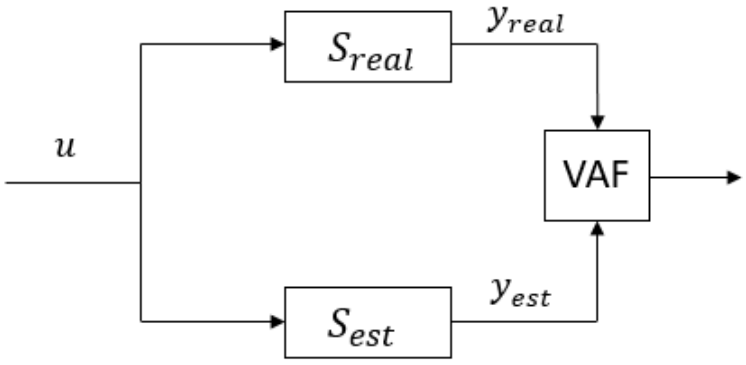

Figure 3.5: VAF parameter.

VAF parameters are involved in both the validation and identification processes. In the latter case the data set is divided into two parts: the first part is used for the dynamic estimation, the second one is manipulated by VAF, which in this peculiar framework is called "cross VAF". In validation, VAF acts on the entire data set, so its result can be considered more significant. Tests are performed in open loop to focus on G_q identification, so the controllers are disabled.

3.2.3 Predictor Based Subspace IDentification

Since controllers shown in Section 4.1 are defined in discrete time domain, G_q is identified in discrete time domain too. Identification processes are carried out with the PBSID method which stands for Predictor Based Subspace IDentification. Such methods fall in the family of Subspace IDentification (SID) that stores inputs and outputs measured data in Hankel matrices. By this structured blocks it is possible to retrieve certain subspaces that are related to system dynamics. Hence canonical A,B,C,D matrices can be estimated by unique knowledge of the input and output measurements.

PBSID are featured by efficiency, simplicity and numerical stability because it relies on linear algebra steps as: RQ, SVD factorisation and linear least squares problems.

The PBSID method structure is well described in [1], which consider a traditional state space model in innovation form:

$$\begin{aligned} x(k+1) &= Ax(k) + Bu(k) + Ke(k) \\ y(k) &= Cx(k) + Du(k) + e(k), \end{aligned}$$

Defining $e(k)$ in function of $y(k)$ and substituting in state space equation it is possible to obtain:

$$\begin{aligned} x(k+1) &= (A - KC)x(k) + (B - KD)u(k) + Ky(k) \\ e(k) &= Cx(k) + Du(k) - y(k), \end{aligned}$$

Now $u(k)$ and $y(k)$ can be collected in $z(k)$ in this way:

$$z(k) = \begin{bmatrix} u(k) \\ y(k) \end{bmatrix},$$

And some new variables can be introduced:

$$\bar{A} = A - KC, \quad \bar{B} = B - KD, \quad \widetilde{B} = \begin{bmatrix} \bar{B} & K \end{bmatrix},$$

Which redefine the state space equation:

$$\begin{aligned} x(k+1) &= \bar{A}x(k) + \bar{B}z(k) \\ y(k) &= Cx(k) + Du(k) + e(k), \end{aligned} \tag{3.2}$$

The data equations for the PBSID algorithm can be derived steping forward the first of equations (3.2) for p, where p is the so-called past window length:

$$\begin{aligned} x(k+2) &= \bar{A}^2 x(k) + \begin{bmatrix} \bar{A}\widetilde{B} & \widetilde{B} \end{bmatrix} \begin{bmatrix} z(k) \\ z(k+1) \end{bmatrix} \\ &\vdots \\ x(k+p) &= \bar{A}^p x(k) + \mathcal{K}^p Z^{k,k+p-1} \end{aligned} \tag{3.3}$$

where $\mathcal{K}^p$ is the extended controllability matrix of the system and $z(k)$ is collected as follow:

$$\mathcal{K}^p = \begin{bmatrix} \bar{A}^{p-1}\widetilde{B} & \bar{A}^{p-2}\widetilde{B} & \dots & \widetilde{B} \end{bmatrix} \tag{3.4}$$

$$Z^{k,k+p-1} = \begin{bmatrix} z(k) \\ \vdots \\ z(k+p-1) \end{bmatrix}.$$

Remembering $\bar{A}$ represents the dynamics of the optimal one-step ahead predictor for the system and therefore has all the eigenvalues inside the open unit circle, thus the term $\bar{A}^p x(k)$ is negligible for sufficiently large values of p and this expression can be obtained:

$$x(k+p) \simeq \mathcal{K}^p Z^{k,k+p-1},$$

As a consequence, the input-output behaviour of the system is approximately given by:

$$\begin{aligned} y(k+p) &\simeq C\mathcal{K}^p Z^{k,k+p-1} + Du(k+p) + e(k+p) \\ &\vdots \\ y(k+p+f) &\simeq C\mathcal{K}^p Z^{k,k+p+f-1} + Du(k+p+f) + \\ &\quad + e(k+p+f), \end{aligned} \tag{3.5}$$

Where f refers to future window length. Let's introduce this kind of matrix notation:

$$\begin{aligned} Y^{p,f} &= \begin{bmatrix} y(k+p) & y(k+p+1) & \dots & y(k+p+f) \end{bmatrix} \\ U^{p,f} &= \begin{bmatrix} u(k+p) & u(k+p+1) & \dots & u(k+p+f) \end{bmatrix} \\ E^{p,f} &= \begin{bmatrix} e(k+p) & e(k+p+1) & \dots & e(k+p+f) \end{bmatrix} \\ X^{p,f} &= \begin{bmatrix} x(k+p) & x(k+p+1) & \dots & x(k+p+f) \end{bmatrix} \\ \bar{Z}^{p,f} &= \begin{bmatrix} Z^{k,k+p-1} & Z^{k,k+p} & \dots & Z^{k,k+p+f-1} \end{bmatrix} \end{aligned} \tag{3.6}$$

Equations (3.3) and (3.5) can be rewritten as:

$$\begin{aligned} X^{p,f} &\simeq \mathcal{K}^p \bar{Z}^{p,f} \\ Y^{p,f} &\simeq C\mathcal{K}^p \bar{Z}^{p,f} + DU^{p,f} + E^{p,f}. \end{aligned} \tag{3.7}$$

Considering $p = f$ case, matrices $C\mathcal{K}^p$ and D are first estimated by solving the least-squares problem:

$$\min_{C\mathcal{K}^p, D} \|Y^{p,p} - C\mathcal{K}^p \bar{Z}^{p,p} - DU^{p,p}\|_F. \tag{3.8}$$

Defining now the extended observability matrix Γ^p as:

$$\Gamma^p = \begin{bmatrix} C \\ C\bar{A} \\ \vdots \\ C\bar{A}^{p-1} \end{bmatrix} \tag{3.9}$$

and noting that the product of Γ^p and $\mathcal{K}^p$ can be written as:

$$\Gamma^p \mathcal{K}^p \simeq \begin{bmatrix} C\bar{A}^{p-1}\widetilde{B} & \dots & C\widetilde{B} \\ 0 & \dots & C\bar{A}\widetilde{B} \\ \vdots & & \\ 0 & \dots & C\bar{A}^{p-1}\widetilde{B} \end{bmatrix}, \tag{3.10}$$

such product can be computed using the estimate $\widehat{C\mathcal{K}^p}$ of $C\mathcal{K}^p$ obtained by solving the least squares problem (3.8). Recalling now that:

$$X^{p,p} \simeq \mathcal{K}^p \bar{Z}^{p,p} \tag{3.11}$$

It is trivial that:

$$\Gamma^p X^{p,p} \simeq \Gamma^p \mathcal{K}^p \bar{Z}^{p,p}. \tag{3.12}$$

Therefore, computing the SVD factorization:

$$\Gamma^p \mathcal{K}^p \bar{Z}^{p,p} = U\Sigma V^T \tag{3.13}$$

an estimate of the state sequence can be obtained as:

$$\widehat{X}^{p,p} = \Sigma_n^{1/2} V_n^T = \Sigma_n^{-1/2} U_n^T \Gamma^p \mathcal{K}^p \bar{Z}^{p,p}, \tag{3.14}$$

Once the states sequence are known, an estimate of C can be computed by solving the least squares problem:

$$\min_C \|Y^{p,p} - \widehat{D}U^{p,p} - C\widehat{X}^{p,p}\|_F. \tag{3.15}$$

The final steps consist of the estimation of the innovation data matrix $E_N^{p,f}$

$$E_N^{p,f} = Y^{p,p} - \widehat{C}\widehat{X}^{p,p} - \widehat{D}U^{p,p} \tag{3.16}$$

and of the entire set of the state space matrices for the system, which can be obtained by solving the least squares problem:

$$\min_{A,B,K} \|\widehat{X}^{p+1,p} - A\widehat{X}^{p,p-1} - BU^{p,p-1} - KE^{p,p-1}\|_F. \tag{3.17}$$

PBSID algorithms are implemented in Predictor-Based Subspace IDentification Toolbox [7]. This toolbox presents several enhancements: for example by singular value analysis, it is able to predict the system order. Moreover, it is possible to calculate the probalistic error bounds around the identified bode diagram. The equality between p and f is imposed, their values have been shifted from 20 to 40 with a double step. Optimal combination is chosen according to best VAF achieved in identification process (cross VAF).

3.3 Results

In each amplitude signal, optimal VAFs are achieved with p equal to 40, so such a value is chosen for all identification processes (in Figure 3.6 $\Delta M = 0.01$ example is reported).

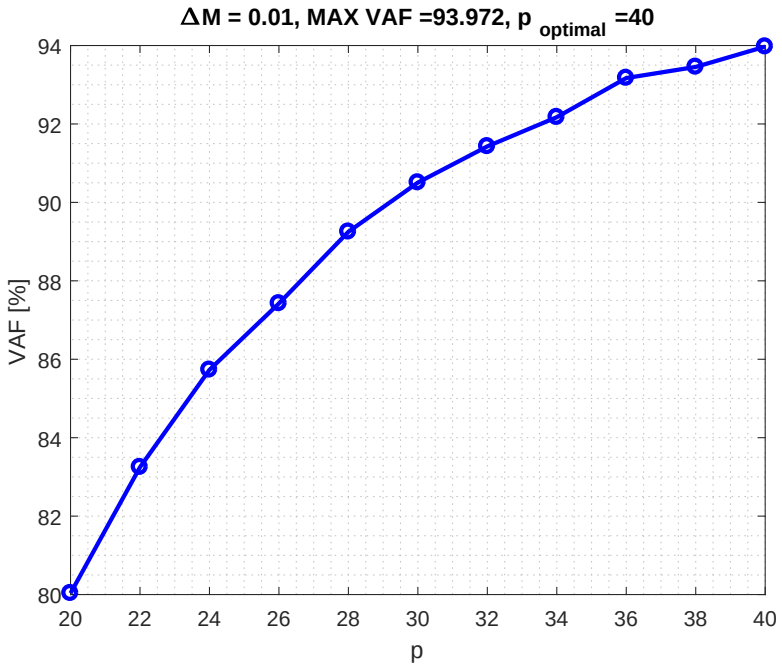

Figure 3.6: Optimal p and f values.

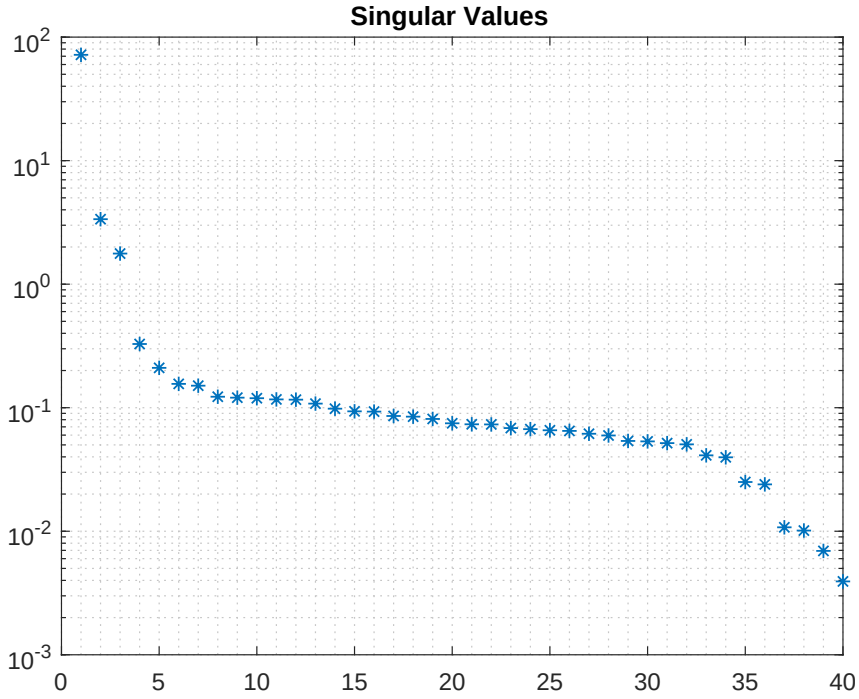

Figure 3.7: Singular values.

Singular values can be analysed in Figure 3.7: it can be asserted the system order is equal to 3.

During the early data elaboration, an inverse response has been recognised so a delay is present. Since negative values persist for 5 samples, the identification process is performed after such a time span. Then a delay term is added to the transfer function expression.

In Figure 3.8 the Bode Diagrams of the identified system are represented, the lowest amplitude signal shows anomalies in terms of gain and peak value.

Amplitude [-]	**CROSS VAF %**
0.01	94
0.007	92
0.004	80

Table 3.2: VAF in identification processes.

In Table 3.2, cross VAFs are listed, while in Table 3.3 VAFs experienced in the validation processes are reported. The lowest amplitude input signal shows the worst VAF values.

In Figure 3.9 are represented the identified Bode diagram (black line) with the probabilistic error bound (grey zone), while in Figure 3.10 poles and zeros map are reported.

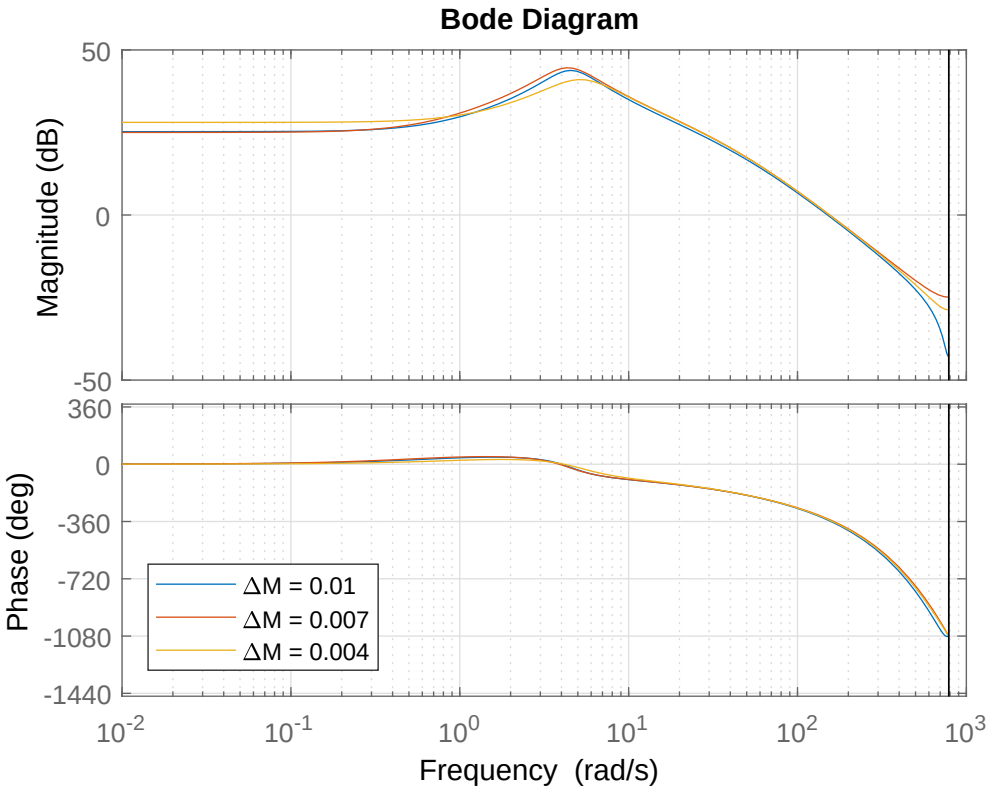

Figure 3.8: Identified system Bode diagram.

Amplitude [-]	**VAF %**
0.01	84
0.01	86
0.01	87
0.007	84
0.007	74
0.007	86
0.004	68
0.004	67
0.004	81

Table 3.3: VAF in validation processes.

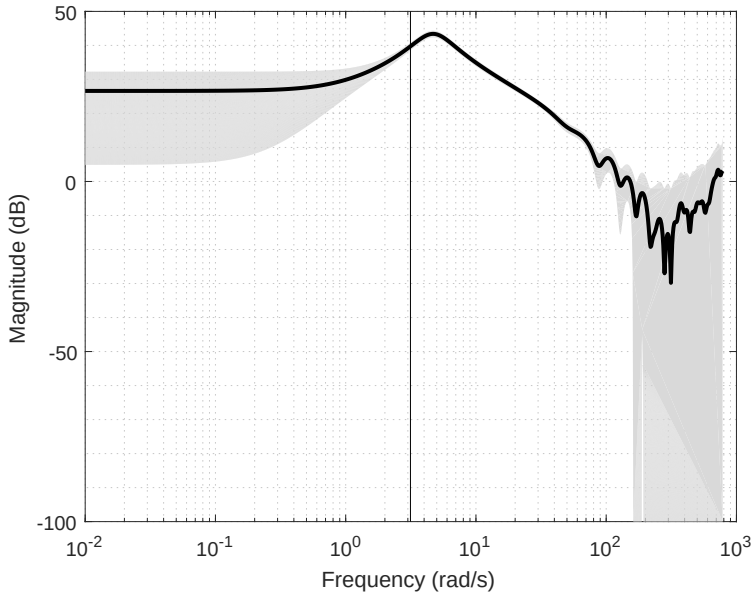

Figure 3.9: Probalistic error bounds around the identified Bode diagrams.

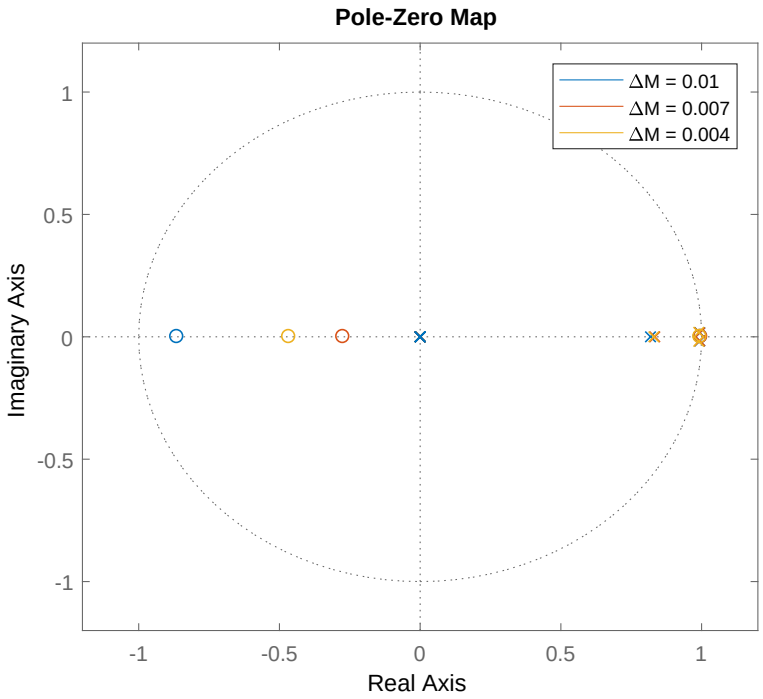

Figure 3.10: Poles and zeroes of identified system.

3.4 Analysis and conclusions

All identification processes result to be successful, but $\Delta M = 0.004$ signal shows several defects in terms of frequency response and VAF. This is probably related to the difficulty of performing moments of such a low amplitude during test. This hypothesis can be confirmed by the fact that optimal VAFs are evaluated in $\Delta M = 0.01$ tests. Signal amplitude could be extended to higher values, but too high oscillations would be achieved and hovering flight condition would be outraged, so results would not be significant.

A valuable dynamics is recognised at 5 rad/s, so input the exciting band supposed in Subsection 3.2.2 can be considered suitable for the identification tests.

Concerning the uncertainties in frequency estimation represented in Figure 3.9, it is clear that they are located where the input signal does not have relevant harmonic content (Figure 3.4), namely at low frequency and above upper band limit (50 rad/s). Poles and zeros represented in Figure 3.10 are located in unit circle area, so the added delay term is proper.

In Figures 3.11, the estimated and the real output can be appreciated.

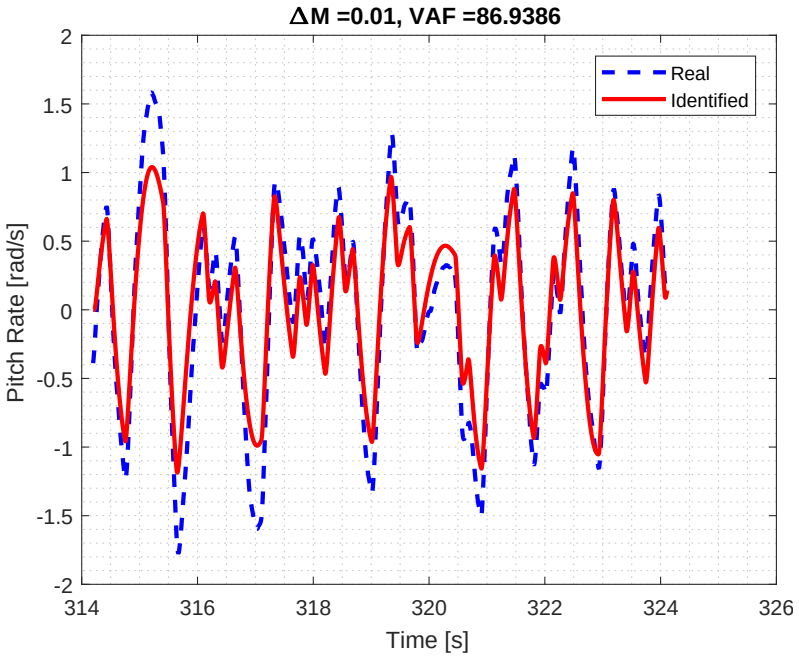

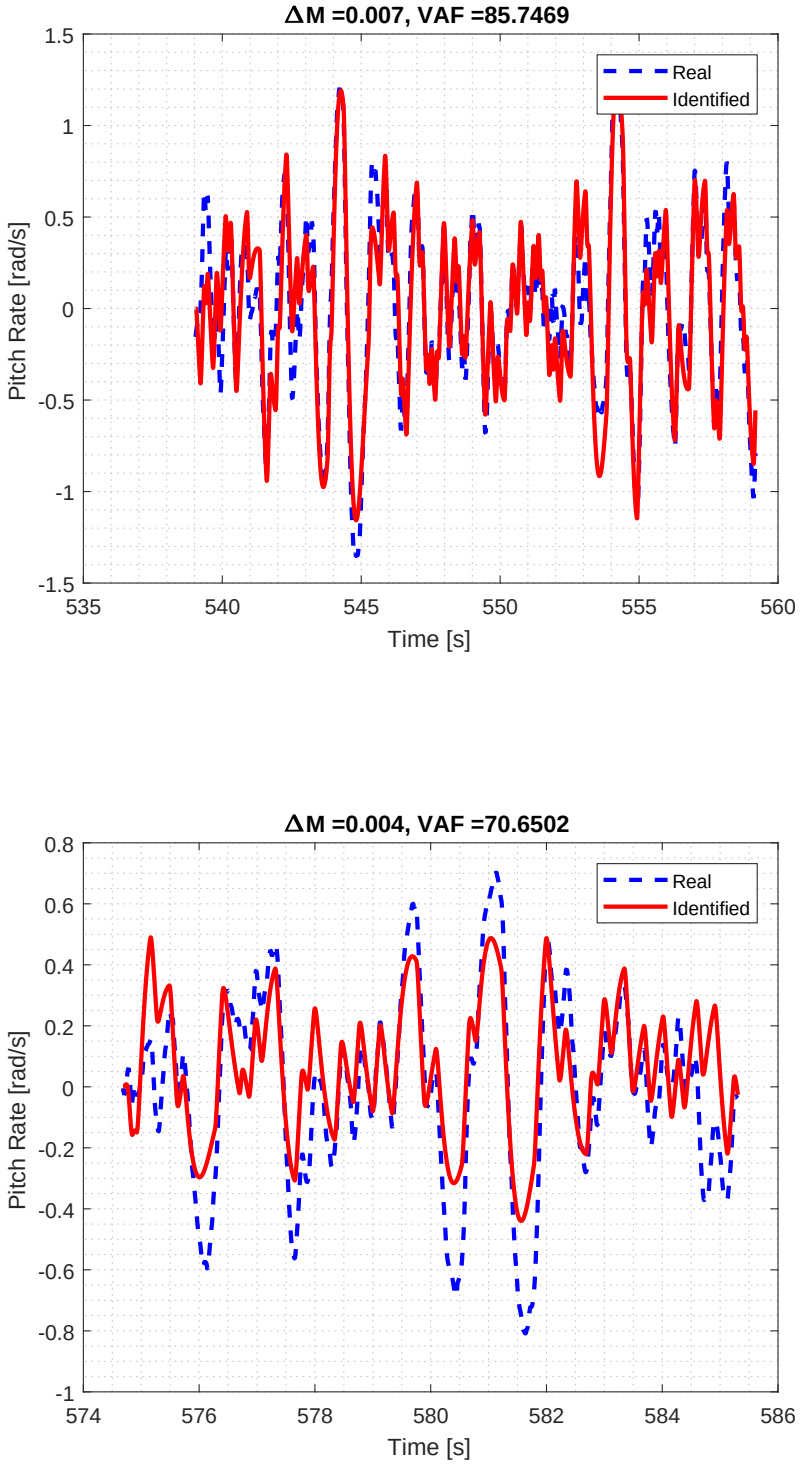

Figure 3.11: Identified and real output.

Chapter 4

Attitude control law design

As a first step, controller parameters have been manually tuned, then the fixed structure H_∞ technique has been adopted to find their optimal values. In this chapter the control architecture is described and the fixed structure H_∞ is introduced. Finally tuned parameters are simulated in Matlab and validated through an experimental campaign performed on the test bed mentioned in Subsection 3.2.1.

4.1 Control architecture

Control actions are exerted by Pixfalcon, which is able to estimate state variables so that the proper inputs are given to actuators. In Figure 4.1 system block scheme is shown and the Pixfalcon location is pointed out with a dash dot blue line.

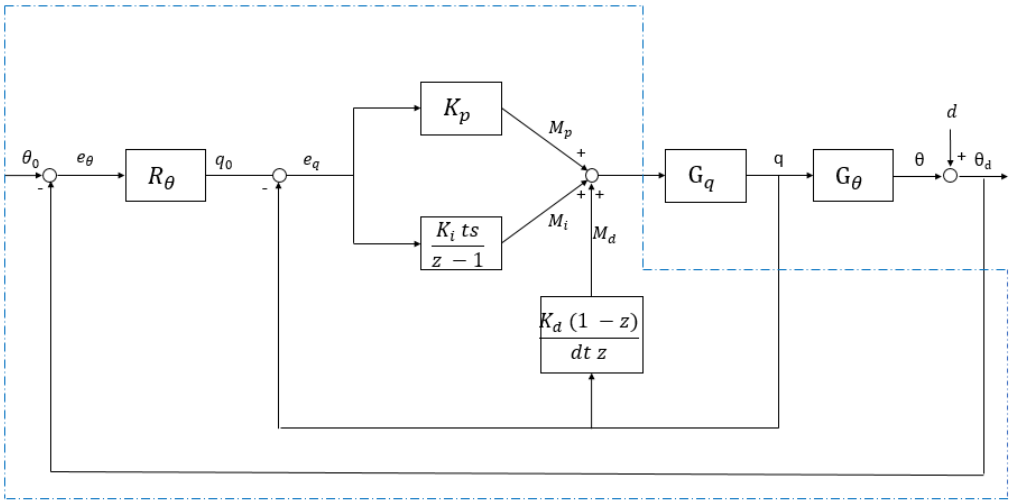

Figure 4.1: Control architecture.

The Pixfalcon control architecture consists of PID controllers defined in discrete time domain and arranged in two loops. The outer loop refers to the pitch angle and is characterised by a proportional controller that receives pitch error e_θ as input and returns pitch rate reference value q_0 as output. The inner loop is associated to the pitch rate and presents a derivative regulator and a parallel connection between a proportional and an integral controllers. The former receives the pitch rate estimation q as input while the latter are fed by pitch rate error e_q. All three controllers contribute to the M moment which feeds G_q.

Controller actions are expressed as 4.1, K and R are respectively the inner and outer PID parameters, ts is sampling time while z refers to Z-transform.

$$\begin{aligned} q_0(t) &= R_\theta \cdot e_\theta(t) \\ M(t) &= \left(K_p + \frac{K_i\ ts}{z-1}\right)\ e_q(t) - \frac{K_d(z-1)}{ts}\ q(t) \end{aligned} \tag{4.1}$$

4.2 Fixed Structure H_∞

As stated in [3], H_∞ theory provides powerful techniques for synthesising controllers in frequency domain. The most interesting advantages offered are summarised in [10]:

- Adaptability to MIMO system: H_∞ techniques can deal with multivariable dynamic systems.
- Robustness: regulators designed with H_∞ achieve properties of closed-loop robustness.
- Optimality: since cost functions are minimised.

Obviously this method also has some drawbacks that have slowed its adoption in industry: for example H_∞ generates monolithic control block characterised by high order whereas control architecture is a typically decentralised collection of simple elements such as gains and PID controllers. That is, order and scheme are fixed and they can not be changed (as ANT-1 case). This limitation is overcome by structured H_∞, which is able to keep into account the pre-existing control characteristics at the cost of converging to a local minima.

Now, H_∞ theoretical base is exposed. In this part, continuous time domain is assumed to keep a general approach, but this technique can be applied in discrete time systems too. At the heart of structured H_∞ is H_∞ norm, which measures peak input/output gain of a stable transfer function:

$$\|H(j\omega)\|_\infty = \max_\omega |H(j\omega)| \tag{4.2}$$

Design requirements such as speed of response, robust stability, disturbance rejection are expressed with weighting transfer functions defined as:

$$\frac{1}{W_T(j\omega)}, \quad \frac{1}{W_S(j\omega)} \quad , \frac{1}{W_Q(j\omega)} \tag{4.3}$$

It's desired that complementary sensitivity T, sensitivity S and control sensitivity Q reflect weighting function shape, which implies:

$$\begin{aligned} |T(j\omega)| &< |\frac{1}{W_T(j\omega)}| \qquad \forall\omega, \\ |S(j\omega)| &< |\frac{1}{W_S(j\omega)}| \qquad \forall\omega, \\ |Q(j\omega)| &< |\frac{1}{W_Q(j\omega)}| \qquad \forall\omega. \end{aligned} \tag{4.4}$$

That can be further manipulated as:

$$\begin{aligned} |T(j\omega)||W_T(j\omega)| &< 1 \qquad \forall\omega, \\ |S(j\omega)||W_S(j\omega)| &< 1 \qquad \forall\omega, \\ |Q(j\omega)||W_Q(j\omega)| &< 1 \qquad \forall\omega \end{aligned} \tag{4.5}$$

Thus, recalling H_∞ norm, (4.5) is satisfied if:

$$\begin{aligned} \|T(j\omega)W_T(j\omega)\|_\infty &< 1, \\ \|S(j\omega)W_S(j\omega)\|_\infty &< 1, \\ \|Q(j\omega)W_Q(j\omega)\|_\infty &< 1 \end{aligned} \tag{4.6}$$

To solve this optimisation problems, the Robust Control Toolbox of Matlab is used, namely *systune* function and *tuning goal* class. These functions tune the PID parameters so that T, S, Q get closer to the weighting functions.

4.3 Choice of weighting functions

The weighting functions are defined in continuous time domain and successively they are converted in discrete time domain. The complementary sensitivity is related to the speed of response by means of its bandwidth, thus the associated weighting function is designed to extend T bandwidth as underlined in Figure 4.2. Its expression can be defined as (4.7):

$$\frac{1}{W_T(j\omega)} = \frac{0.001j\omega + 64}{j\omega + 42,67} \tag{4.7}$$

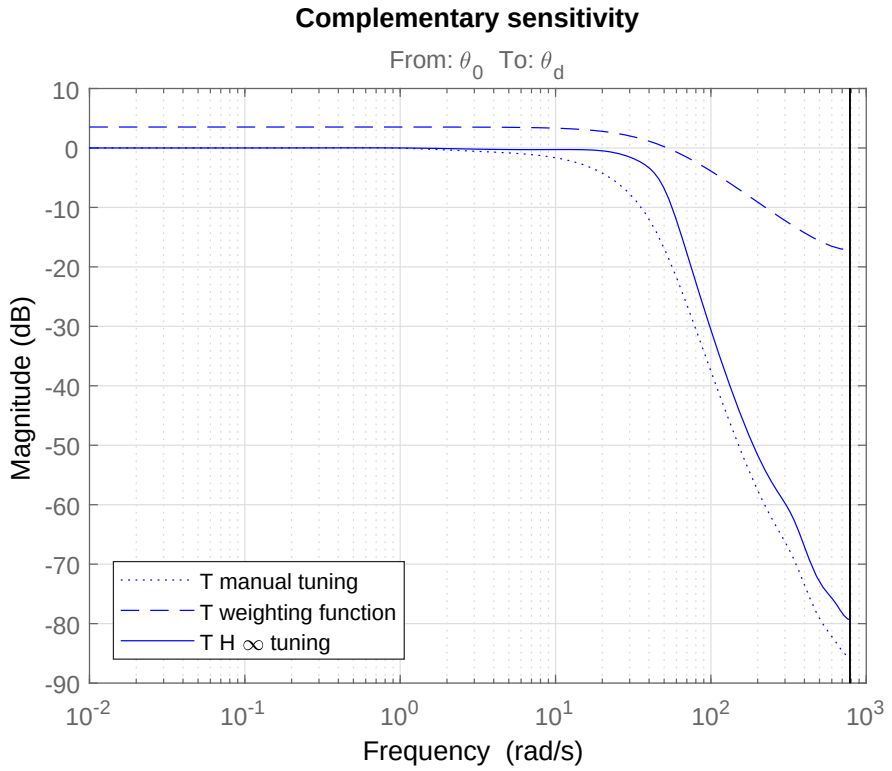

Figure 4.2: Complementary sensitivity and associated weighting function.

Furthermore, one can design a sensitivity weighting function to reject disturbances in specific range of frequency, as reported in 4.8:

$$\frac{1}{W_S(j\omega)} = \frac{1.5j\omega + 0.024}{j\omega + 24} \tag{4.8}$$

H_∞ leads to a sensitivity characterised by disturbance rejection until 12 rad/s accompanied by a proper attenuation as shown in Figure 4.3.

The control sensitivity aim is to avoid actuator stress, imposing weight outside actuator bandwidth. That is, the lowest $\frac{1}{W_Q}$ amplitude values are achieved outside this frequency gap. This characteristic is expressed in (4.9) and can be recognised in Figure 4.4.

$$\frac{1}{W_Q(j\omega)} = \frac{j\omega + 23.26}{0.52j\omega + 0.01} \tag{4.9}$$

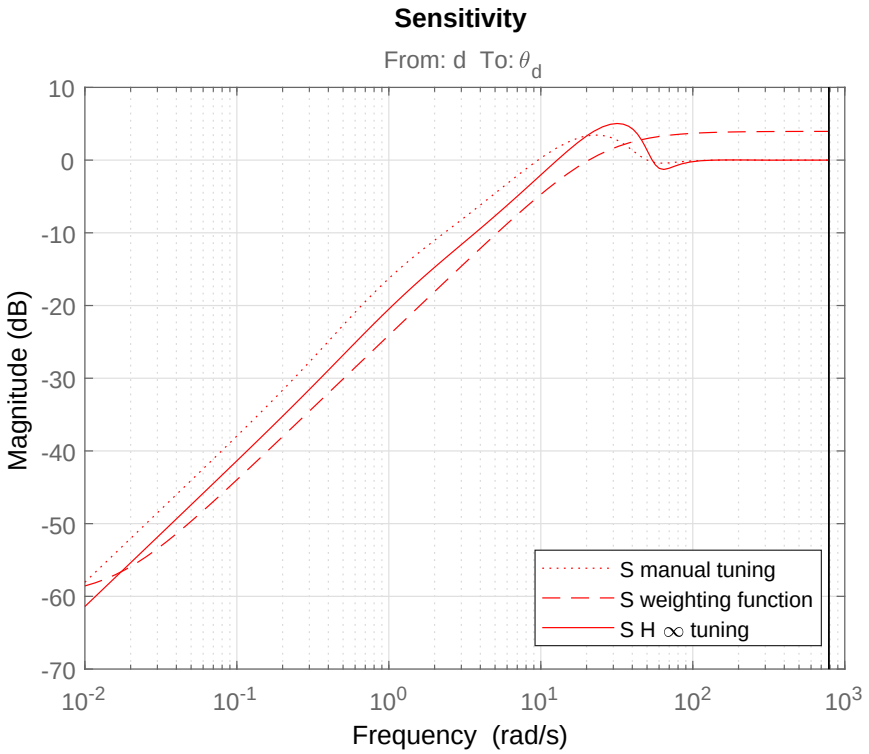

Figure 4.3: Sensitivity and associated weighting function.

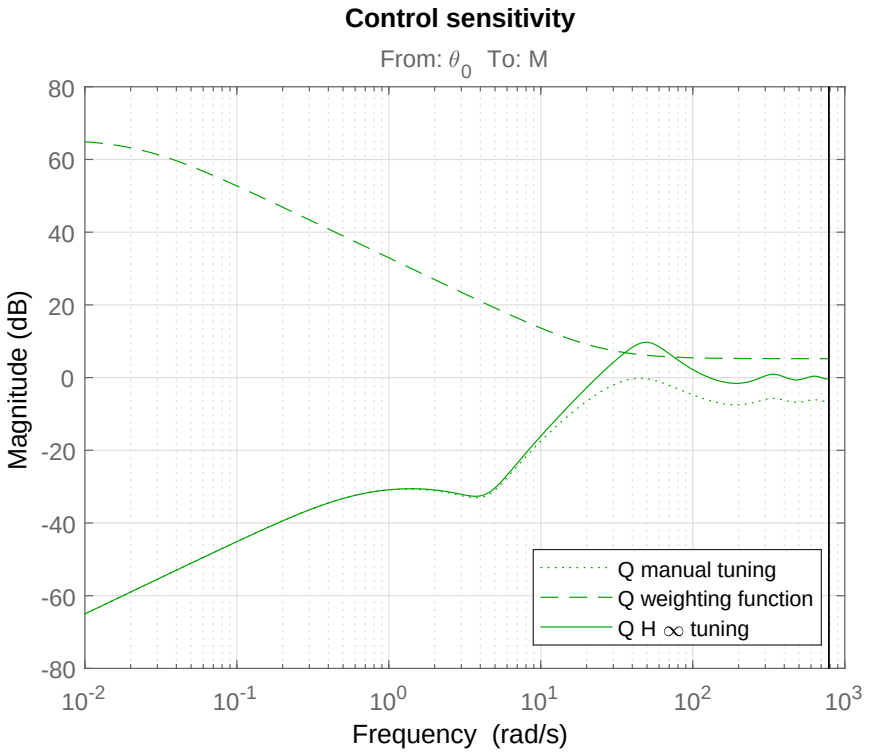

Figure 4.4: Control sensitivity and associated weighting function.

4.4 Validation results

H_∞ technique leads to the PID parameters listed in Table 4.1:

Controller	Initial parameter	Tuned parameter
R_θ	8	11.75
K_p	0.06	0.085
K_i	0.1	0.2138
K_d	0.001	0.0014

Table 4.1: PID parameters.

Such values are simulated through Matlab and verified in a real double step test as reported in Figure 4.6.

In Figure 4.5 the responses achieved in real tests are compared in a zoom of the step function.

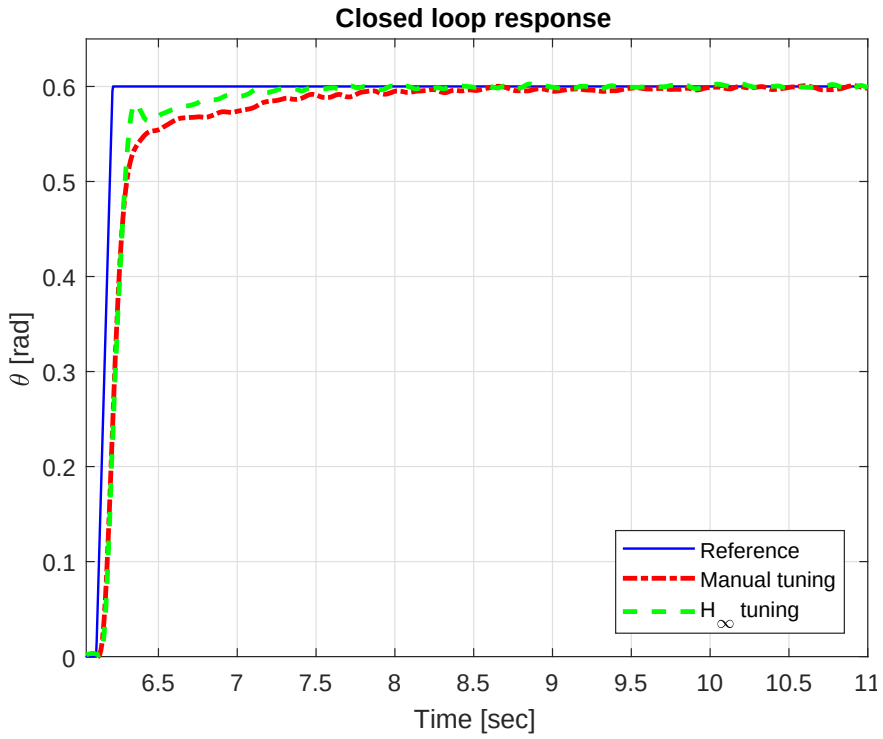

Figure 4.5: Responses comparison.

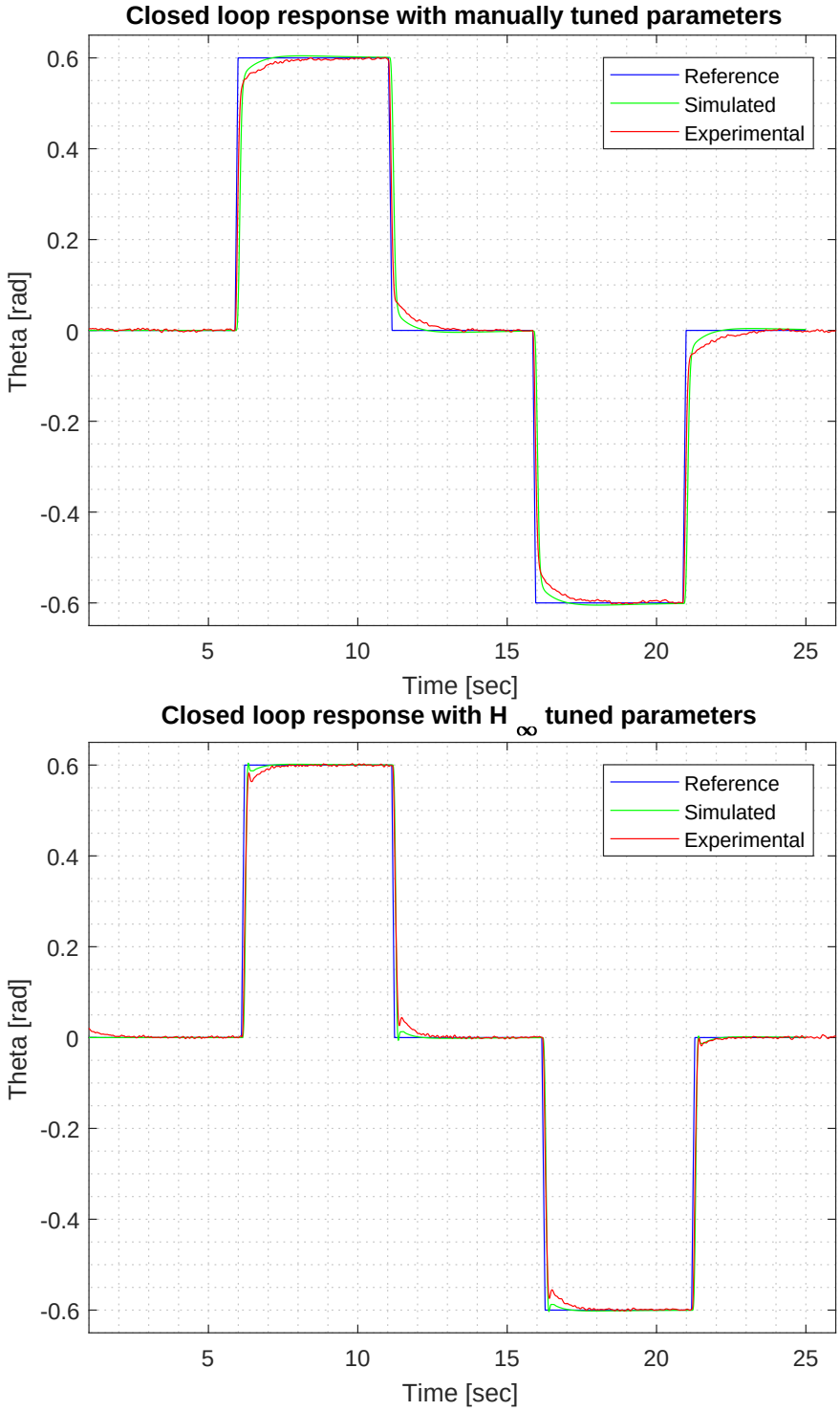

Figure 4.6: Double step test.

4.5 Analysis and conclusions

Some satisfactory results can be recognised. In Figure 4.2, the complementary sensitivity bandwidth is extended, in fact, as reported in Figure 4.5, H_∞ controllers lead to a faster time of response.

Moreover, analysing Figure 4.7, a zoom of Figure 4.6 at step input peak, a similarity between the simulated and experimental responses can be appreciated.

However, it should be remembered that a local minima has been detached, so this controller parameter set does not represent the best solution. Indeed some drawbacks can be noticed in the shape of H_∞ transfer function. In Figure 4.3 sensitivity shows an amplified over peak, while in Figure 4.4 the control sensitivity exceeds the related weighting function in a small frequency range. Such defects are considered acceptable since noise does not lead to relevant attitude excursions as reported in Figure 4.7. Concerning control sensitivity, the QAV1306-3100KV motors are designed for drone races, in which aggressive manoeuvres are performed. So they are able to withstand sudden rotor acceleration.

Thus, the H_∞ parameter advantages offset aforementioned drawbacks and the results are considered satisfactory.

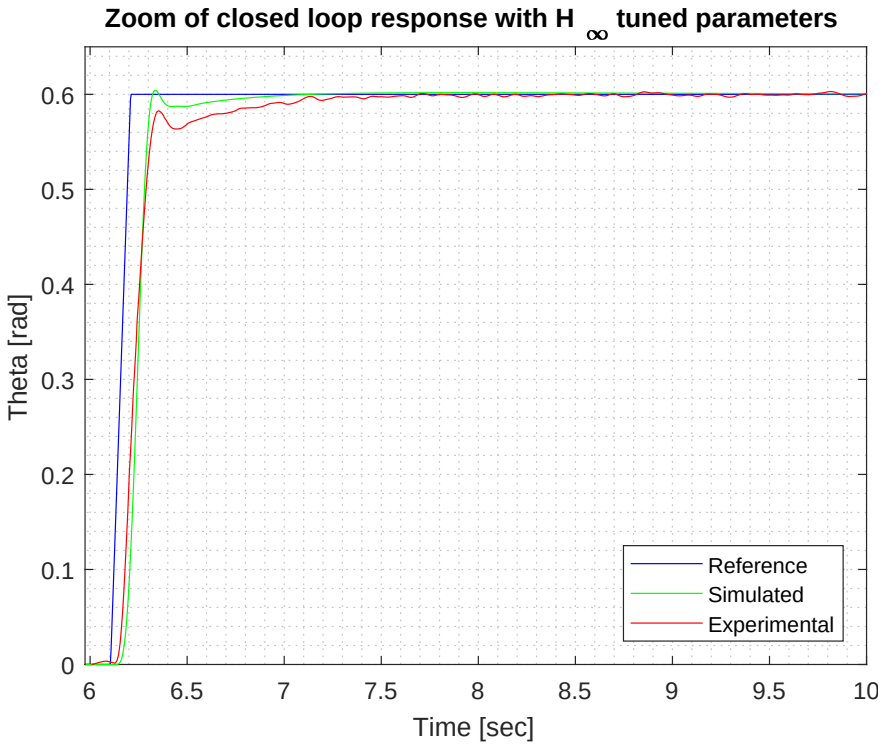

Figure 4.7: Zooms of achieved responses after step input.

Conclusions

ANT-1 weights only 230 grams, it is small scale and provided with a powerful Raspberry companion computer. Its reduced dimension make ANT-1 suitable for swarming flight, moreover, by Raspberry computational capability it could communicate and cooperate with other MAVs.

Its motors provide bigger thrust than eCalc calculations. In fact, a 2.4 thrust to weight value was expected, but, as actuator analysis shown, a 2.9 value can be obtained at full throttle. This thrust capability can be involved in aggressive manoeuvres.

Identification processes leads to high VAF values and similar models, hence they can be considered accurate.

Finally, H_∞ results to be a powerful tool in control design. ANT-1 shows a faster time of response. This enhancement is confirmed by our flight test pilot too.

Thus, it can be asserted that a MAV with capabilities of aerial collective system can be realised and that it is possible to start working on its applications.

Further developments

ANT-1 is in a preliminary phase, there is still much work to be done, for example:

- Identification flight tests have to be planned and executed to compare its identified model with the one obtained in ground tests.
- Aerial collective system feasibility has to be demonstrated. The collaboration and coordination with other MAVs have to be verified, implementing and testing the related software enhancements as relative positioning or traffic collision avoidance system.
- ANT-1 is ready to be tested in cluttered environment, establishing routes and waypoint navigation.

Table of acronyms

Acronym	Description
DoF	Degree of freedom
ESC	Electronic speed controller
FCU	Flight control unit
FPV	First person view
GPS	Global positioning system
GPU	Graphic processing unit
MAV	Micro aerial vehicle
MTOW	Maximum take off weight
PBSID	Predictor based subspace identification
RBS	Random binaries signal
RC	Remotely controlled
RPV	Remotely piloted vehicles
SID	Subspace identification method
SoC	System on a chip
UAV	Unmanned aerial vehicle
VAF	Variance accounted for

Bibliography

[1] A. Chiuso. The role of autoregressive modeling in predictor-based subspace identification. *Automatica*, 43(3):1034–1048, 2007.

[2] ENAC. *Remotely piloted aerial vehicle regulation.* 2016.

[3] Pascal Gahinet and Pierre Apkarian. Structured hinf synthesis in matlab. *IFAC Proceedings Volumes*, 44(1):1435–1440, 2011.

[4] M. Giurato. Design, integration and control of a multirotor uav platform. 2015.

[5] L. J. Gordon. *Principles of helicopter aerodynamics with CD extra.* Cambridge university press, 2006.

[6] J. Grasmeye and M. Keennon. Development of the black widow micro air vehicle. *Progress in Astronautics and aeronautics*, 195:519–535, 2001.

[7] I.Houtzager, J. van Wingerden, and M. Verhaegenl. Varmax-based closed-loop subspace model identification. In *Decision and Control, 2009 held jointly with the 2009 28th Chinese Control Conference. CDC/CCC 2009. Proceedings of the 48th IEEE Conference on*, pages 3370–3375. IEEE, 2009.

[8] M. Keennon and J. Grasmeyer. Development of the black widow and microbat mavs and a vision of the future of mav design. In *AIAA/ICAS International Air and Space Symposium and Exposition: The Next*, volume 100, pages 14–17, 2003.

[9] C. Melhuish and J. Welsby. Gradient ascent with a group of minimalist real robots: Implementing secondary swarming. In *Systems, Man and Cybernetics, 2002 IEEE International Conference on*, volume 2, pages 509–514. IEEE, 2002.

[10] S. Panza. Hinfguide's documentation. `https://flyart.gitlab.io/hinfguide/`.

[11] J. Zufferey, T. Stirling S. Hauert, J. Roberts S. Leven, and D. Floreano. Aerial collective systems. Technical report, Pan Stanford, 2013.